Molecular Therapy
Nucleic Acids
Original Article

miR-107 represses *DMPK* and is sequestered by CUG repeats triggering the MSI2/miR-7 pathogenesis axis in myotonic dystrophy

N. Moreno,[1,2,3,11] M. Sabater-Arcis,[1,2,3,11] J. Espinosa-Espinosa,[4] L. Mulet-Rivero,[5] E. García-España,[5] J. González-García,[5] D. Seoane-Miraz,[6,7] M.J.A. Wood,[6,7] M.A. Varela,[6,7] J. Ohana,[8] T. Sevilla,[3,9,10] M. Perez Alonso,[1,2,3] A. Bargiela,[3,9,12,13] and R. Artero[1,2,3,12]

[1]Human Translational Genomics Group, University Institute for Biotechnology and Biomedicine (BIOTECMED), University of Valencia, Av. Dr. Moliner 50, 46100 Valencia, Spain; [2]INCLIVA Biomedical Research Institute, Av. Menendez Pelayo 4, 46010 Valencia, Spain; [3]CIBERER ISCIII, Av. Monforte de Lemos 3-5, 28029 Madrid, Spain; [4]Experimental and Applied Biomedicine Research Group, Health Sciences Faculty, Universidad Particular Internacional SEK, Alberto Einstein S/N, Quito 170120, Ecuador; [5]Department of Inorganic Chemistry, Instituto de Ciencia Molecular (ICMOL), University of Valencia, Catedrático José Beltrán Martínez, 2, 46980 Valencia, Spain; [6]Department of Paediatrics, Institute of Developmental and Regenerative Medicine (IDRM), University of Oxford, Roosevelt Dr. Headington, Oxford OX3 7TY, UK; [7]MDUK Oxford Neuromuscular Centre, Oxford, UK; [8]Sorbonne Université, Inserm, Institut de Myologie, Centre de Recherche en Myologie, Batiment Babinski, GH Pitié-Salpétrière 47 bd de l'Hôpital, 75651 Paris Cedex, France; [9]Neuromuscular and Ataxias Research Group, Health Research Institute Hospital La Fe (IIS La Fe), Av. de Fernando Abril Martorell, 106, 46026 Valencia, Spain; [10]Department of Medicine, University of Valencia, Av. Blasco Ibañez 15, 46010 Valencia, Spain

Myotonic dystrophy type 1 (DM1) is a multisystem genetic disorder characterized by muscle disease, including muscle atrophy partially originating from excessive autophagy. We have previously demonstrated that excessive Musashi-2 (MSI2) repressed the biogenesis of miR-7, which derepressed autophagy, ultimately contributing to muscle atrophy, but the root cause of MSI2 dysregulation is unknown. Herein, we investigate the intricate role of miR-107 in DM1 pathogenesis, focusing on its involvement in the MSI2>miR-7>autophagy axis as this microRNA (miRNA) directly regulates MSI2. We found that in DM1, miR-107 function is impaired because expanded CUG repeats sequester it, causing an increase in the expression of its targets, including MSI2. Through different experimental approaches, including luciferase reporter assays, differential scanning fluorimetry, and electrophoretic mobility shift assay (EMSA), we confirm that miR-107 directly binds to CUG repeats in mutant *DMPK* transcripts. DMPK posttranscriptional regulation by miR-107 was also demonstrated. Modulation of miR-107 in a DM1 cell model context significantly affects its downstream targets, MSI2 and miR-7, thus decreasing excessive autophagic markers and restoring pathological phenotypes such as ribonuclear foci and impaired fusion capacity. These findings underscore the critical role of miR-107 in regulating the MSI2>miR-7>autophagy axis and support this miRNA as a promising therapeutic target for correcting muscle dysfunction in DM1.

INTRODUCTION

Myotonic dystrophy type 1 (DM1) is an autosomal dominant genetic disorder characterized by a broad spectrum of multisystem manifestations encompassing myotonia, muscle weakness, cardiac abnormalities, and cognitive deficits.[1–3] The disease arises from the expansion of unstable trinucleotide (CTG) repeats in the 3′ untranslated region (3′ UTR) of the *DM1 protein kinase* (*DMPK*) gene.[4] These expanded CUG repeats initiate a pathological cascade by sequestering RNA-binding proteins from the muscleblind-like splicing regulator (MBNL) family. MBNL1 and MBNL2 proteins play a crucial role in post-transcriptional regulation, including alternative splicing, polyadenylation, microRNA (miRNA) biogenesis, and mRNA stability.[5,6] In addition, the pathophysiology of DM1 is enhanced by dysregulation of CUGBP Elav-like family member 1 (CELF1), a splicing factor antagonistic to MBNL that is stabilized in DM1 due to its hyperphosphorylation by protein kinase C.[7] Altogether, MBNL sequestration by ribonuclear foci and CELF1 stabilization contribute to alternative splicing disruption.[8–10] Dysfunctional autophagy and ubiquitin-proteasome activity, coupled with AMP-activated protein kinase (AMPK) downregulation, disruption of the serine/threonine protein kinase B/forkhead box O (AKT/FOXO) signaling pathway and GSK3β activation, further contribute to the muscle pathology characteristic in DM1 patients.[11]

Received 20 May 2024; accepted 2 June 2025;
https://doi.org/10.1016/j.omtn.2025.102584.

[11]These authors contributed equally

[12]These authors contributed equally

[13]Present address: INCLIVA Biomedical Research Institute, Av. Menendez Pelayo 4, 46010 Valencia, Spain

Correspondence: A. Bargiela, INCLIVA Biomedical Research Institute, Av. Menendez Pelayo 4, 46010 Valencia, Spain.
E-mail: abargiela@incliva.es

miRNAs are a class of small non-coding RNAs critical for post-transcriptional gene regulation. These molecules bind to the 3′ UTR of target mRNAs, thereby modulating their stability and translation.[12,13] Recent research has underscored the pivotal role of miRNA-mediated post-transcriptional regulation in shaping the molecular landscape of DM1; for example, miR-23b and miR-218 negatively regulate MBNL1 and 2 protein synthesis,[14–16] miR-206 is involved in muscle maturation,[17] miR-16 colocalizes with *DMPK* ribonuclear foci,[18] and miR-322/-503 with a seed region complementary to CUG repeats was proved to directly and specifically target expanded CUG repeats in the DM1 cells. Ectopic expression of miR-322/-503 in DM1 muscle cells leads to significant improvements in myoblast differentiation and repression of ribonuclear foci formation and aberrant alternative splicing.[19]

In recent years, autophagy—the cellular process responsible for degrading and recycling cellular components—has emerged as a critical pathway implicated in muscular disorders, and its importance in maintaining muscle homeostasis and addressing atrophy-related pathways in DM1 has been highlighted.[11,20–23] miR-7 is a repressor of autophagy[24] and its biogenesis is regulated by Musashi homolog 2 (MSI2) and HuR antigen (HuR).[19] MSI2, an RNA-binding protein, binds via HuR to the terminal loop of pri-mir-7-1, inhibiting the biosynthesis of the mature form of the miRNA.[25,26] MSI2 is an alternative splicing factor and mRNA translational and stability regulator.[27,28] In DM1, increased MSI2 expression triggers the MSI2>-miR-7>autophagy axis, contributing to dysregulated autophagy and muscular atrophy in DM1.[29,30] Notably, MSI2 is upregulated in DM1 muscle cells and biopsies, and upon restoring its levels, we observed rescue of miR-7 and atrophy-related gene expression of autophagy and ubiquitin-proteasome system (UPS) markers.[30] Additionally, experimental induction of DM1-like phenotypes was noticed upon AAV-mediated overexpression of murine Msi2 in skeletal muscle in neonatal human skeletal actin long repeat (HSA^{LR}) mice. This overexpression prompted autophagic flux, altered the expression of critical autophagy proteins, and led to increased central nuclei, diminished myofiber area, and compromised muscle strength.[29]

MSI2 is directly regulated by miR-107.[31] Indeed, the miRNA family of miR-107, which consists of miR-15/-107/-16, has garnered attention for its potential implications in DM1. Earlier research has demonstrated that *DMPK* is directly regulated by miR-206, miR-148a, and miR-16. By extension, therefore, other miR-107 family members may also modulate disease pathology.[18]

This study aimed to elucidate the causes leading to MSI2 overexpression in DM1. We hypothesized that it could be due to miR-107 sequestration by expanded CUG repeats in the *DMPK* mutant transcripts. In this way, miR-107 would be deprived of its normal regulatory function, leading to the derepression of MSI2 in a DM1 context. Understanding the regulatory interplay between mutant *DMPK*, miR-107, and MSI2 is vital in understanding the autophagic dysregulation and resultant muscle atrophy observed in DM1.

RESULTS

miR-107 function is depleted in DM1

Based on previous studies[17–19] and bioinformatics predictions from miRWalk and miRTarBase-v9.0[32,33] (scores of 0.92 and 0.95, respectively), we hypothesized that miR-107 could form base pairs with the expanded CUG repeats in the 3′ UTR of *DMPK* (Figure 1A). This sequestration would result in the derepression of miR-107 targets, including MSI2. To investigate this, we analyzed the expression levels of predicted miR-107 targets using RNA sequencing (RNA-seq) data from DM1 biopsies and transdifferentiated myotubes (TDMs) derived from immortalized fibroblasts.[14,23,34] Initially, we performed differential gene expression analysis to identify all significantly dysregulated transcripts (adjusted p value <0.05). Predicted miR-107 targets were subsequently selected from these significantly dysregulated genes, and their expression levels were systematically compared between control (CNT) and DM1 conditions (Table S1). To assess the statistical significance of the observed changes, we applied Fisher's exact test to evaluate the proportion of upregulated miR-107 targets relative to downregulated genes in each biological condition (biopsies, 4 or 8 days differentiated TDMs). This analysis revealed a significantly higher number of upregulated miR-107 targets (Figure 1B) across all three kinds of samples. Notably, MSI2 was among the miR-107 targets upregulated in TDMs differentiated for 4 and 8 days under pathological conditions (Figure 1C). Overall, these findings further support our hypothesis of impaired miR-107 repressor activity in the DM1 context. We speculated that miR-107 sequestration would result in significant accumulation of this miRNA in the nuclear fraction of DM1 myotubes. To test our hypothesis, the nucleus and cytoplasm of control and DM1 immortalized myotubes were separated, and the miRNome of each fraction was sequenced. This allowed us to determine the distribution of miR-107 in each compartment. As shown in the interaction graph (Figure 1D), miR-107 subcellular localization shifted from predominantly cytoplasmic in control cells to nuclear in cells derived from DM1 patients. This is illustrated by the intersecting lines connecting each sample in both fractions, with blue lines representing controls and gray lines indicating pathological condition. In healthy controls, miR-107 was primarily detected in the cytoplasm, as expected for a functional miRNA. In contrast, DM1 cells exhibited a redistribution, with a significantly higher proportion of miR-107 localized in the nucleus. These findings support our hypothesis that miR-107 accumulates in the nucleus of DM1 cells due to its sequestration by expanded CUG repeats. To determine whether, in addition to altered subcellular distribution, miR-107 total levels were also affected, we analyzed miR-107 expression in transdifferentiated myotubes (TDMs) at days 0 and 7 of differentiation, as well as in immortalized myotubes and muscle biopsies from DM1 patients using RT-qPCR (Figures 1E–1G). In the case of CNT TDMs, we observed an upward trend in miR-107 levels upon differentiation. This effect was evident in the case of CNT myotubes, where miRNA expression was 70% higher in differentiated cells. Additionally, in both TDMs and myoblasts, healthy control and disease model cells exhibited similar miR-107 levels at day 0 of differentiation (Figures 1E and 1F). However, after 7 days of differentiation, a significant decrease in miRNA expression

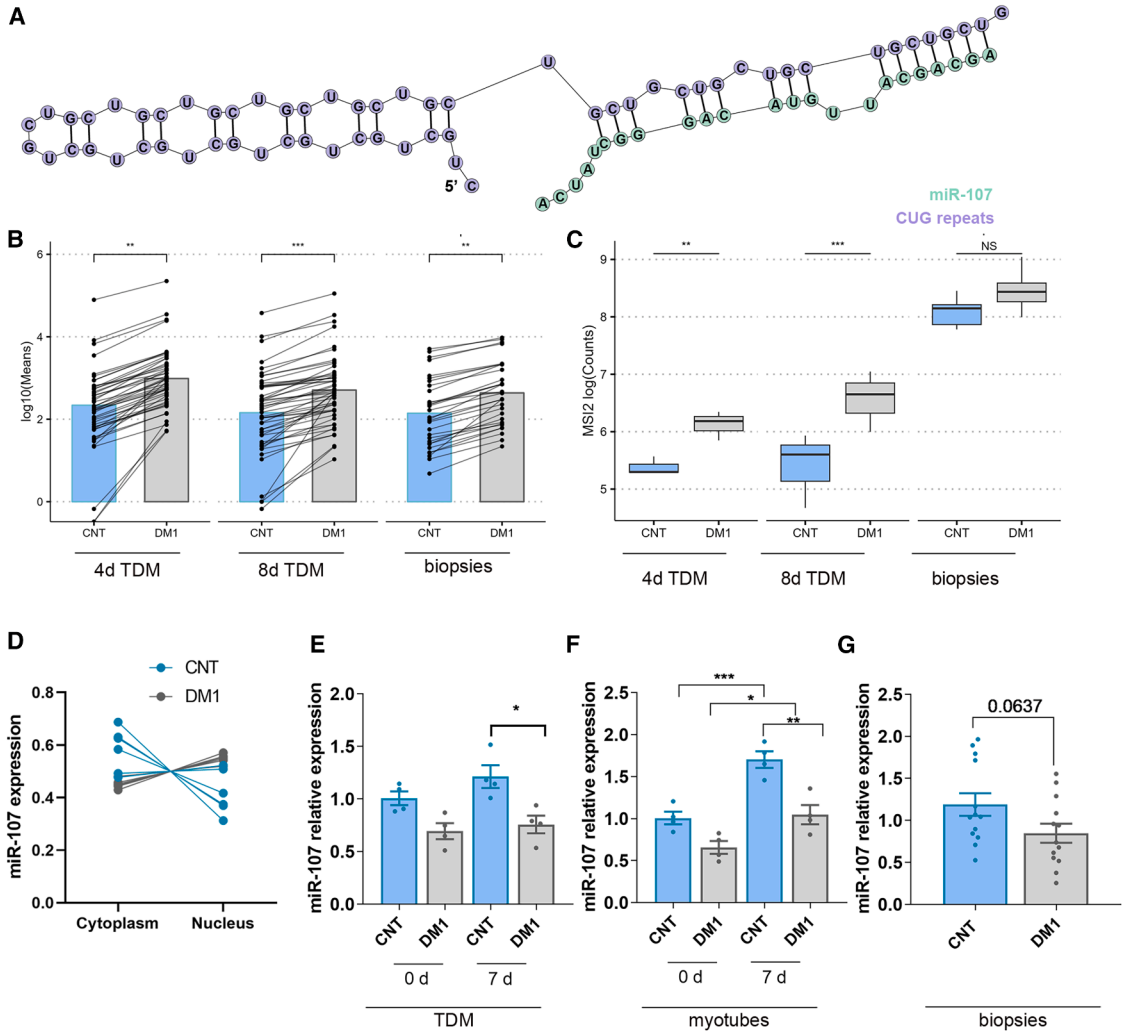

Figure 1. miR-107 dysregulation in DM1

(A) Illustration depicting the complementarity between miR-107 and 20 CUG triplets. (B) Representation of the mean expression of miR-107 targets in DM1 TDMs differentiated over 4 ($n = 3$) or 8 days ($n = 3$) and in patient biopsies ($n = 5$ CNT and 22 DM1) was plotted as a bar. Individual gene expression was denoted as a point. Counts were represented on a logarithmic scale. To evaluate enrichment in upregulated genes, a binary contingency table between up- and downregulated genes, miR-107 and non-miR-107 targets was constructed to perform a Fisher's exact test for each type of sample. Only genes with a log fold change over 0 and an adjusted p value < 0.05 were considered. (C) The boxplot represents normalized *MSI2* expression levels (log-transformed normalized counts). Statistical analysis was performed using the quasi-likelihood F-test implemented in the edgeR package, with statistical significance denoted as NS $p > 0.05$, $^{**}p < 0.01$, and $^{***}p < 0.001$. The horizontal line within each box represents the median expression level, while the upper and lower edges of the box correspond to the third and first quartiles, respectively, capturing the interquartile range (IQR). Whiskers extend to the smallest and largest values within 1.5 times the IQR, and any points beyond these are considered outliers. (D) Interaction plot showing the relative expression of miR-107 in the nucleus and cytoplasm from CNT and DM1 myoblasts obtained from RNA-seq data ($n = 5$). (E–G) Quantification of relative miR-107 levels in TDMs at 0 and 7 ($n = 4$) days of differentiation, in immortalized myoblasts at day 0 and 7 of differentiation ($n = 4$), and biopsies ($n = 14$) by RT-qPCR. The bar graphs show mean ± SEM. $^{*}p < 0.05$, $^{***}p < 0.001$, and $^{****}p < 0.0001$ according to Fisher's exact test (B), Student's t test (G), or one-way ANOVA test (E and F) with post hoc tests when necessary.

was detected in the model cells. Since differentiation defects have been reported in DM1,[35] we further examined whether impaired differentiation could contribute to miRNA dysregulation (Figures S1AS1D). A reduction in fusion capacity of 61% and 65% was detected in DM1 TDMs and myotubes, respectively (Figures S1AS1D). This suggests that the decrease in miR-107 expression in patient-derived cells is not solely a direct consequence of the pathology but is also influenced by differentiation defects, which reduce the percentage of myotubes formed.

Finally, the reduction in miR-107 in patient-derived muscle biopsies was marginally non-significant (p value = 0.06) (Figure 1G). These findings suggest that miR-107 levels decrease while its subcellular localization changes in the presence of mutant *DMPK*. This effect

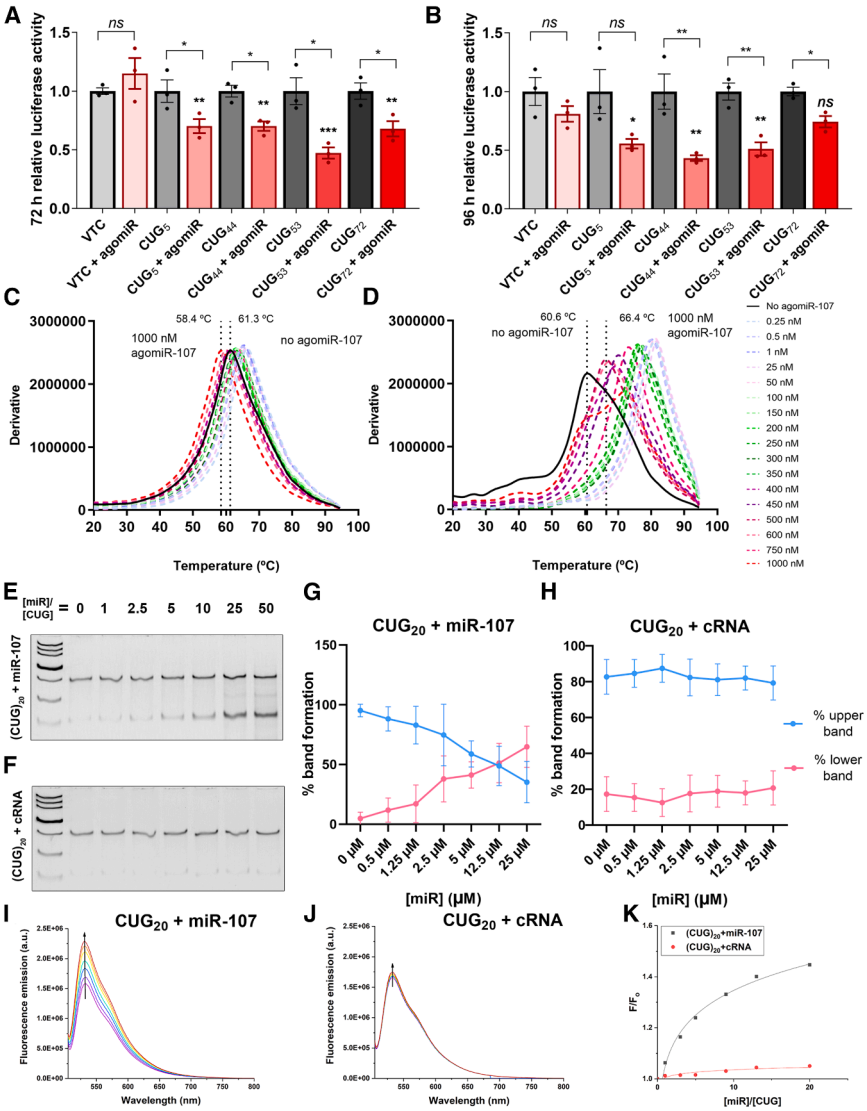

Figure 2. miR-107 represses DMPK expression and directly binds CUG repeats

(A and B) Relative luciferase activity measured after 72 h (A) or 96 h (B) of co-transfection of HEK293 cells with reporter constructs containing 0 (VTC), 5, 44, 53, or 72 CTG repeats, along with 100 nM miR-107 mimic. The asterisks above the bars indicate the level of statistical significance obtained by comparing the condition marked with the asterisk to the VTC + agomiR group (*$p < 0.05$, **$p < 0.01$, and ***$p < 0.001$), according to a one-way ANOVA test followed by and Tukey's HSD post hoc correction. Asterisks over the brackets indicate comparisons of each condition with the corresponding CUG repeats without the miR-107 mimic (*$p < 0.05$ and **$p < 0.001$, according to Student's t test). Firefly luciferase activity was normalized to *Renilla* luciferase. The bar graphs show mean ± SEM. calculated from three independent experiments. (C and D) Normalized fluorescence intensity of RiboGreen fluorescence versus temperature at different miR-107 concentrations with CUG_{20} (C) or CGA_{20} as a control (D). (E and F) Representative EMSA blots of CUG_{20} with increasing concentrations of miR-107 (E) or control RNA (cRNA) (F). (G and H) Quantification of the percentage of each band in EMSAs combining CUG_{20} probe, and miR-107 mimic (G) or cRNA control (H). The results presented in EMSA assay are the average of three (G) and two (H) independent experiments. (I and J) Fluorimetric titration of CUG_{20}-TO with agomiR-107 (I) or cRNA (J) in NaCac buffer (10 mM NaCac [pH 7.4], λ_{exc} = 495 nm). Each spectrum corresponds to different ratios between 2 µM CUG_{20} and agomiR-107 and cRNA ranging from 0.25 (purple) to 20 (red) equivalents. (K) Plot of the ratio between fluorescence emission and initial fluorescence emission (F/Fo) versus molar ratio ([miR]/[CUG_{20}]).

is likely due to its sequestration by CUG repeats, as supported by the upregulation of miR-107 target genes in DM1 samples.

miR-107 directly targets CUG repeats

We observed changes in the subcellular localization of miR-107 under pathological conditions, along with the derepression of its targets. Thus, suggesting both direct binding of miR-107 to CUG repeats and a functional deficit of the miRNA. To further investigate whether the interaction between miR-107 and expanded CUG repeats leads to *DMPK* repression, we conducted a luciferase reporter assay to assess miR-107 binding to CUG repeats fused to a luciferase reporter gene.[18] For this, HEK293 cells were transfected with reporter constructs carrying 5, 44, 53, or 72 CTG triplets—where the latter two fall within the pathogenic range of DM1—fused to firefly luciferase, along with a miR-107 mimic. A decrease in firefly luciferase activity upon miRNA binding to the repeats suggested that miR-107 targets *DMPK* and regulates its translation. A control vector lacking CTG repeats (VTC) was also included. Comparison of cells co-transfected with CUG reporters and agomiR-107 versus those transfected only with the construct carrying the CTG repeats (red vs. gray bars) revealed a significant reduction in luciferase activity at both 72 h (Figure 2A) and 96 h (Figure 2B), indicating the ability of miR-107 to repress reporter expression (asterisks in brackets). Moreover, comparison of VTC transfected with agomiR versus co-transfection with luciferase sensors expressing different CUGs lengths (red bars) revealed a reduction in luciferase (asterisk above the bars), suggesting again that miR-107 regulates *DMPK*. At 72 h (Figure 2A), the decrease in luminescence was around 30%, except for CUG_{53} (50% reduction), while at 96 h (Figure 2B), the miRNA effect was more pronounced, generally reducing luciferase expression by 50%. The correlation between CUG repeat expansion and luciferase repression was limited, likely due to technical factors. Notably, untreated HEK293 cells already express endogenous miR-107, as reported in the Zembu miRNA expression atlas.[36] This fact may have constrained the degree of additional reporter repression upon

miR-107 overexpression, potentially reaching a silencing plateau. Additionally, efficient co-transfection may not have occurred in a significant fraction of the cells. Finally, in the VTC construct transfected with agomiR-107, luciferase activity was not repressed compared to the VTC without the mimic, confirming that the inhibitory effect of miR-107 requires the presence of CUG repeats.

Mutant *DMPK* sequester miR-107, preventing its normal function

Luciferase reporter assays indicate that miR-107 binds to CUG repeats and inhibits protein translation via RNA-induced silencing complexes (RISC). However, in the nucleus, miR-107 may also interact directly with CUG repeats, independently of any specific protein. To test this hypothesis, we studied the interaction between CUGs and miR-107 *in vitro*.

Differential scanning fluorimetry (DSF) has been established as a powerful technique for studying biomolecular interactions *in vitro*.[37,38] Thus, we performed a conventional DSF assay to assess miR-107 binding to CUG repeats. The experiment involved incubating a fixed concentration of CUG_{20} probe (600 nM) with varying concentrations of agomiR-107 (0.5–1,000 nM). To determine whether miR-107 specifically recognized CUG sequences rather than a general secondary structure, we included CGA_{20} as a control probe, as it shares structural similarities with CUG repeats.[37] Interestingly, at miR-107 concentrations above 400 nM, the melting temperature (Tm) of double-stranded CUG_{20} decreased markedly (Figure 2C), indicating destabilization of its secondary structure. In contrast, the CGA_{20} probe exhibited the opposite trend, even at low miR-107 concentrations (Figure 2D). To further quantify miR-107 binding to CUG_{20} we performed an electrophoretic mobility shift assay (EMSA), maintaining a constant concentration of CUG_{20} RNA while increasing miR-107 levels (Figures 2E–2H) and their technical controls (Figure S2). We observed two bands corresponding to CUG_{20}, the upper corresponding to the double-stranded RNA and the lower formed by unstructured RNA conformation. The intensity of the lower band increased concomitantly with increasing concentrations of miRNA. Analysis of the intensities of both bands allowed us to quantify the interaction of miR-107 with CUG_{20} as a DC50 (50% dissociation concentration) of 11.6 μM (Figures 2E and 2G). To confirm specificity, the experiment was conducted with a control RNA lacking complementarity to the CUG_{20} (cRNA). In this case, the experiments showed no shift in the CUG_{20} bands, suggesting that the miR-107 can effectively and specifically interact with the CUG_{20} secondary structures and unfold them (Figures 2F and 2H). These results were confirmed by fluorescent indicator displacement (FID) assay aimed to explore the interaction dynamics between miR-107 and the toxic RNA.[38] Thiazole orange (TO) is an asymmetric cyanine dye that intercalates into double-stranded RNA or DNA, exhibiting strong fluorescence upon binding.[39] This property makes TO a useful tool for monitoring RNA-RNA interactions. As expected, adding a miR-107 mimic to a solution containing CUG_{20} RNA led to a concentration-dependent increase in fluorescence intensity (Figures 2I–2K). In contrast, titrating increasing amounts of cRNA into the CUG_{20} solution resulted in only a minimal fluorescence increase, further supporting the specificity of miR-107 binding to CUG repeats.

CUG repeats exert an inhibitory effect on DMPK expression mediated by miR-107

Based on luciferase reporter experiments and direct binding assays, we hypothesized that miR-107 represses *DMPK* expression in DM1 cells. Transcriptomic data supported our hypothesis, showing reduced *DMPK* expression in DM1 TDMs differentiated for 4 and 8 days (Figure S4A). To further explore this regulation, we treated 7-day-differentiated DM1 TDMs with agomiR-107. Prior to defining experimental conditions, we assessed the toxicity profile of the miR-107 mimic in the same cells (Figure 3A). A concentration of 100 nM (first vertical dotted line in Figure 3A) was selected for subsequent experiments, as approximately 70% of cells remained viable at this concentration, with the TC_{50} occurring at 1,000 nM. We found that DMPK expression was significantly reduced in DM1 TDMs compared to control TDMs at both transcript and protein levels, as previously reported[14] (Figures 3B and 3C). Furthermore, no differences in *DMPK* levels were observed between CNT cells at 0 and 7 days of differentiation, suggesting that the observed differences in DMPK between healthy and DM1 cells is not due to a different myoblast/myotube ratio but is rather a disease-associated phenotype (Figures S1E and S1F). Notably, miR-107 supplementation yielded a significant additional decrease in *DMPK* mRNA in DM1 cells (Figure 3B) that reached 50% reduction in DMPK protein levels by western blot (Figures 3C and S3A). Treatment of control cells with 100 nM agomiR showed similar effects to those obtained in DM1 cells (Figures 3D and S3B), thus suggesting that miR-107 also regulates DMPK under physiological conditions.

To confirm that miR-107 downregulates DMPK through direct and functional binding to the CUG sequence within the 3′ UTR of *DMPK*—and to exclude the possibility of miRNA targeting another region of the transcript—we analyzed DMPK expression in edited DM1 immortalized myotubes. Using CRISPR-Cas9, DM1 myoblasts were edited to excise the expanded CTG repeats, resulting in a phenotypic rescue of DM1 cells.[40] After 7 days of differentiation, both edited lines (DM1 3B11Δ/Δ and DM1 4A3Δ/Δ) showed a marked derepression of DMPK compared to the isogenic unedited line, which retained 2,600 CTG repeats (Figures 3F–3H). The significant increase in DMPK expression upon repeat excision demonstrated the repressive effect of the expanded CTG triplet. Notably, DMPK protein was undetectable in unedited DM1 myotubes, making its derepression even more apparent after CTG repeat excision (Figures 3E, 3F, and S3C). Further supporting this hypothesis, we treated both unedited and edited DM1 cells with 100 nM agomiR-107. While miR-107 supplementation led to a substantial reduction in DMPK levels in DM1 TDMs and a milder effect in CNT cells (Figures 3B and 3C), edited DM1 cells remained unresponsive to miR-107 treatment at both the transcript and protein levels (Figures 3E, 3F, and S3C). This result strongly supports the notion that miR-107 regulates DMPK via its interaction with CUG repeats.

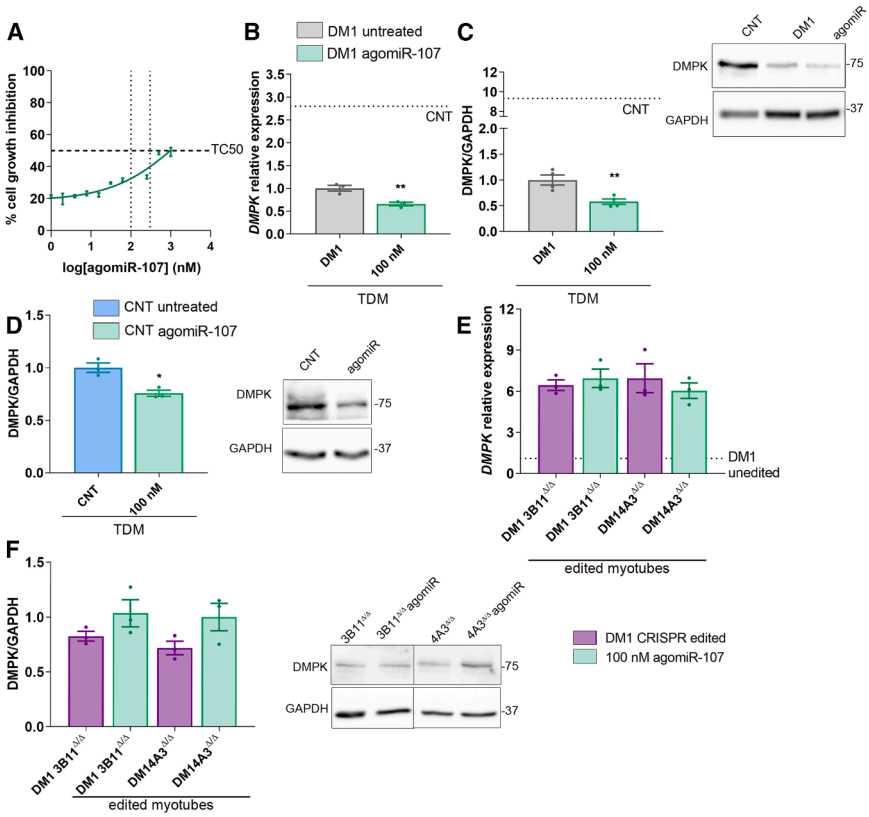

Figure 3. CUG repeats exert a repressive effect on DMPK expression mediated by miR-107

(A) Cell growth inhibition assay by MTS/PMS method. DM1 TDM were transfected with agomiR-107 ranging from 1 nM to 1 μM (n = 4). TC50 (2,106 nM) was obtained using the least-squares non-linear regression model. Vertical dashed lines denote agomiR concentrations used for further studies: 100 and 300 nM. (B–F) Quantification of *DMPK* transcripts (B and E) or protein (C, D, and F) in DM1 (B and C) or CNT (D) TDM differentiated for 7 days (n = 3/4) and CRISPR-edited myotubes (3B11$^{\Delta/\Delta}$ and 4A3 $^{\Delta/\Delta}$) (E and F) untreated or treated with 100 nM agomiR-107 (n = 3). Unedited myotubes are missing in (F) since DMPK protein levels were below the detection capacity of the technique. Representative blots are next to protein quantification graphs. *DMPK* transcripts were normalized to the endogenous expression of the mean of *GAPDH* and *GPI*, while DMPK protein was relative to GAPDH expression. The bar graphs show mean ± SEM. *p < 0.05 and **p < 0.01 according to Student's t test (B, C, and D) or one-way ANOVA test (E and F) and post hoc tests when necessary.

In this context, it is also possible that miR-107 interacts with nuclear DMPK, which may act as a miRNA sponge.

miR-107 mediates foci reduction and MBNL1 subcellular localization

To determine whether miR-107 inhibition of *DMPK* affects ribonuclear foci, we analyzed this phenotype in DM1 TDMs treated with increasing concentrations of agomiR-107 using fluorescent *in situ* hybridization. As a validation control, we included chromomycin, a well-established foci-reducing compound,[41] as a positive control, while TDMs from healthy donors served as a negative control. miR-107 supplementation at 25, 100, or 150 nM resulted in a significant reduction in the average number of foci per cell (Figure 4A). Additionally, the proportion of diseased cells lacking detectable foci increased significantly within the 25–250 nM concentration range (Figure 4B), demonstrating a dose-dependent response to agomiR-107 treatment. Notably, this response followed a classic bell-shaped hormetic pattern, indicative of a concentration-dependent effect. Considering these findings, we explored MBNL1 colocalization with the aberrant *DMPK* transcripts. For this purpose, we immunodetected MBNL1 and ribonuclear foci in control, DM1, and DM1 cells treated with increasing concentrations of agomiR-107 using both TDMs and immortalized myotubes (Figures 4C and 4D). Next, we quantified the colocalization of signals corresponding to ribonuclear foci and MBNL1 (Figures 4E and 4F). Our data revealed significantly reduced colocalization of foci with MBNL1 in treated TDM cells upon 100 or 300 nM agomiR treatment (Figures 4C and 4E). However, no discernible response was noted upon myotube treatment (Figures 4D and 4F). The consistent reduction in foci observed upon miR-107 supplementation supports the hypothesis that miR-107 interacts with *DMPK*, leading not only to DMPK downregulation but also to the disruption of ribonuclear foci and the release of MBNL1. Interestingly, while TDM treatment with 300 nM agomiR did not further decrease foci number, it did affect MBNL1 sequestration within these structures. This suggests that, in the nucleus, miR-107 may bind mutant *DMPK* RNA in competition with other molecules that are also sequestered by the expanded CUG repeats.

Impaired MSI2>miR-7>autophagy axis in DM1 is restored upon miR-107 replenishment

To elucidate the molecular dynamics associated with DM1 and the involvement of miR-107 in the MSI2>miR-7>autophagy pathway, we treated DM1 TDMs and immortalized myoblasts with 100 and 300 nM agomiR-107. Thus, counteracting the functional deficiency of miR-107 due to its sequestration by mutant *DMPK* transcripts. We first assessed MSI2 levels in treated cells (Figures 5A–5D). Our results confirmed a reduction in both protein (Figures 5A–5C and S5A) and transcript (Figure 5D) levels in TDMs treated with either concentration of the miRNA mimic. In immortalized myotubes, a significant decrease in MSI2 protein levels was observed at both doses (Figures 5A, 5C, and S5B); however, no significant effect was detected at the transcript level (Figure 5D). Next, we examined miR-7 levels (Figure 5E), which were expected to increase upon MSI2 repression since miR-7 biogenesis is inhibited by MSI2 through its binding to the terminal loop of pri-mir-7-1.[26] Treatment

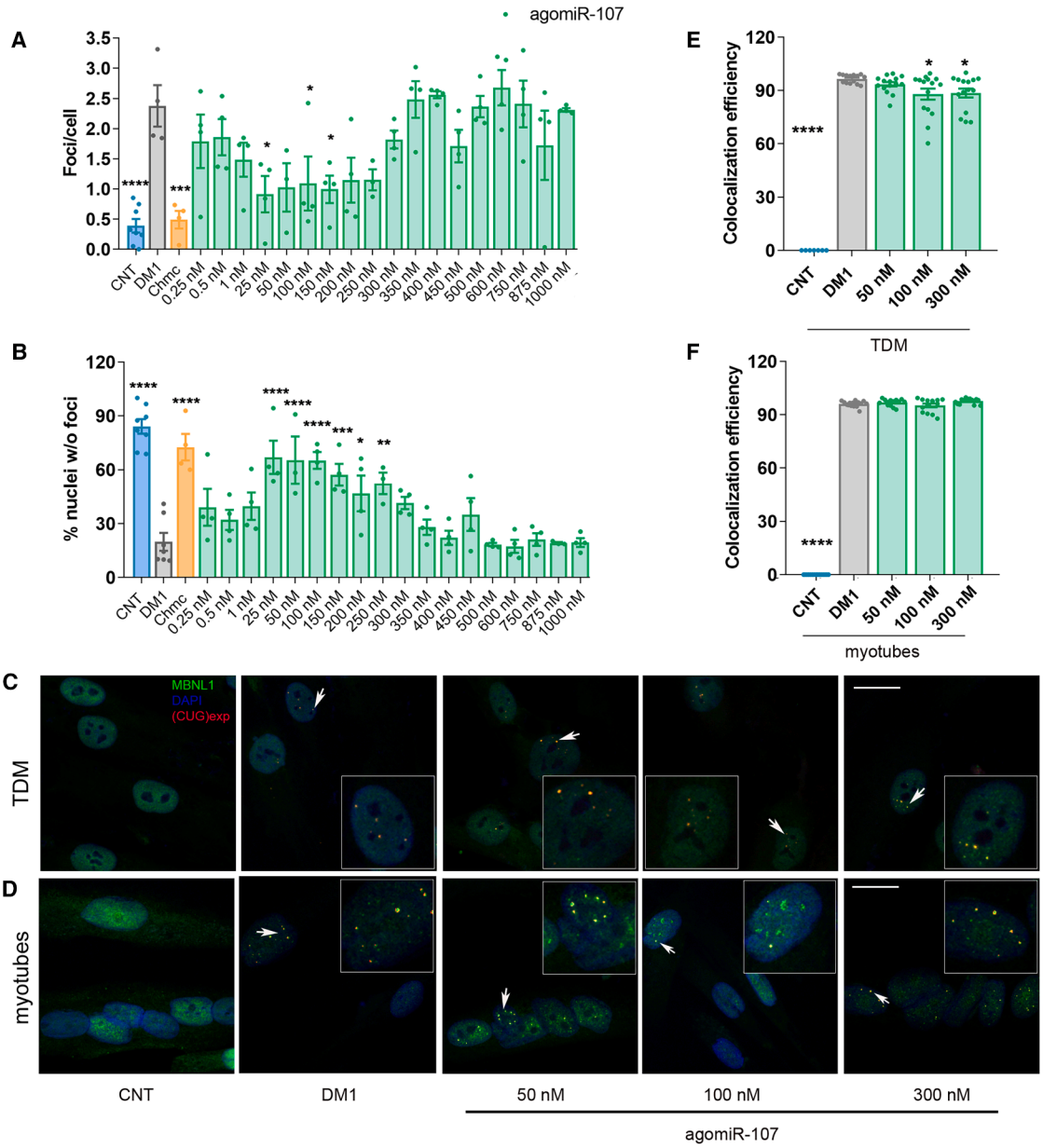

Figure 4. Modulating miR-107 levels in DM1 ameliorates foci-related phenotypes

(A and B) Quantification of foci number per cell (A) and the percentage of nuclei without foci (B) obtained from *in situ* hybridization in CNT and DM1 TDM untreated or treated with the indicated concentrations of miR-107 mimic. Chromomycin (chmc) (4 μM) was used as a positive control. (C and D) Representative confocal images of MBNL1 (green) immunostaining and fluorescent *in situ* hybridization showing the ribonuclear foci using a CAG probe (red) in control and DM1 TDM (C) or immortalized myotubes (D) untreated or supplemented with the indicated concentrations of agomiR-107. Nuclei were counterstained with DAPI and white arrows indicate ribonuclear foci. Between 100 and 200 nuclei were analyzed per condition. Scale bars, 20 μm. (E and F) Percentage of colocalization between foci (measured as Cy3 positive pixels) and MBNL1 (FITC positive pixels) and normalized to the total number of pixels in TDM (E) or immortalized myotubes (F) per image. The bar graphs show mean ± SEM. $^{*}p < 0.05$, $^{**}p < 0.01$, $^{***}p < 0.001$, and $^{****}p < 0.0001$ according to a one-way ANOVA test and Tukey's HSD post hoc test when necessary (A, B, E, and F).

with 100 nM agomiR-107 significantly increased miR-7 expression in TDMs and myotubes, indicating a positive modulation of miR-7. However, no effect was detected when cells were supplemented with the highest dose of miRNA mimic. Notably, miR-7 increase and MSI2 reduction correlated negatively.

Since MSI2 promotes excessive autophagic activity by repressing miR-7, which in turn regulates key autophagy-related genes such as ATG4A and ATG7,[24,25] we evaluated whether miR-107 influences autophagy in DM1 cells. We supplemented DM1 TDMs with 100 or 300 nM agomiR-107 and assessed the expression of key

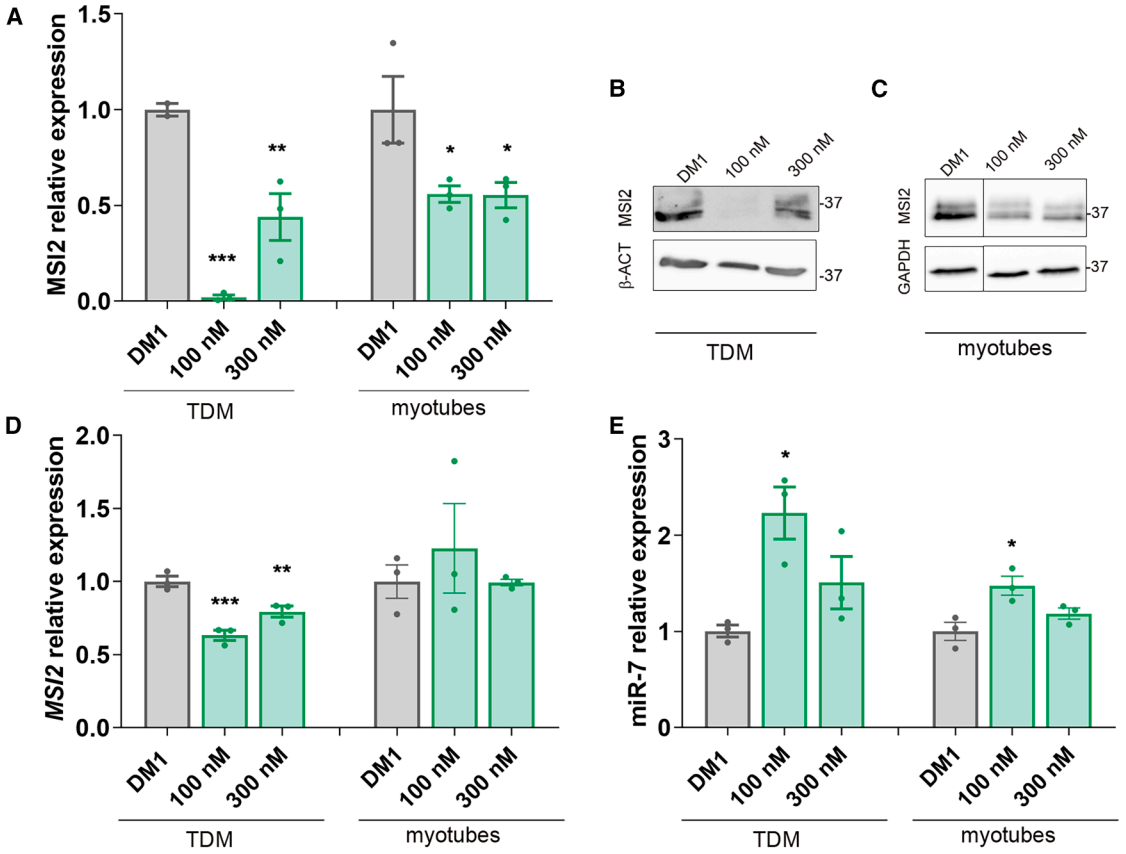

Figure 5. AgomiR-107 treatment in DM1 cells restores MSI2 and miR-7 levels

(A–C) Quantification (A) and representative blots (B and C) of MSI2 protein in 7-day-differentiated TDM and immortalized myotubes treated with miR-107 mimic at the indicated concentrations ($n = 3$). (D and E) Quantification of MSI2 transcripts (D) and relative miR-7 (E) levels by RT-qPCR in the same experimental conditions as in (A). miR-7 quantification is relative to endogenous *U1* and *U6* levels, and *MSI2* transcripts were normalized to endogenous expression of the mean of *GAPDH* and *GPI*. Asterisks indicate statistically significant differences between untreated DM1 cells and the conditions indicated in the graphs. The bar graphs show mean ± SEM. $^{*}p < 0.05$, $^{**}p < 0.01$, and $^{***}p < 0.001$, according to one-way ANOVA test and Tukey's HSD post hoc test when necessary (A, D, and E).

autophagy-related proteins. Treatment with 100 nM agomiR-107 resulted in a partial rescue of the autophagic phenotype, as evidenced by reductions in ATG4 (Figures 6A, 6B, and S6A) and ATG7 (Figures 6C, 6D, and S6B) toward control-like levels. This suggests a decrease in autophagic activity, likely impacting autophagosome formation and cellular degradation dynamics. Consistent with this, P62 levels increased following 100 nM agomiR-107 treatment (Figures 6E, 6F, and S6C), reflecting a disruption in cargo degradation, as P62 facilitates the shuttling of ubiquitinated cargo to autophagosomes.[42] At 300 nM level, however, no significant effects were detected, underlining the importance of finding an effective dose in treatment. In DM1 myotubes, the effects mirrored those observed in TDMs, except for ATG7, which remained unchanged at 100 nM despite a significant reduction in TDMs at the same dose (Figures 6G–6L and S7).

As a complement to protein quantifications, we performed LysoTracker staining, which enables visualization of lysosomes, a key indicator of autophagic activity[43] (Figures 7A and 7B). In control healthy cells, minimal red LysoTracker staining was observed in both analyzed cell lines, aligning with the expected outcome, as healthy cells typically exhibit well-regulated and basal autophagic levels. This observation contrasts with the heightened autophagy observed in cells derived from DM1 patients. Treatment with agomiR-107 revealed a noteworthy reduction in lysosome count, indicating a decrease in lysosomal activity. This observation was confirmed by quantification of lysosomes in each condition, revealing a total recovery of the phenotype upon agomiR supplementations either at 100 or 300 nM (Figures 7C and 7D), supporting the findings from ATG4, ATG7, and P62 expression analyses. Collectively, these results reinforce the role of miR-107 in modulating autophagy and highlight its potential relevance in DM1 pathogenesis.

Supplementation with agomiR-107 improves fusion index and diameter in cellular models

To further explore the impact of miR-107 modulation in the context of DM1, we investigated its effect on the fusion index and diameter of DM1 cellular models. These parameters measured the differentiation

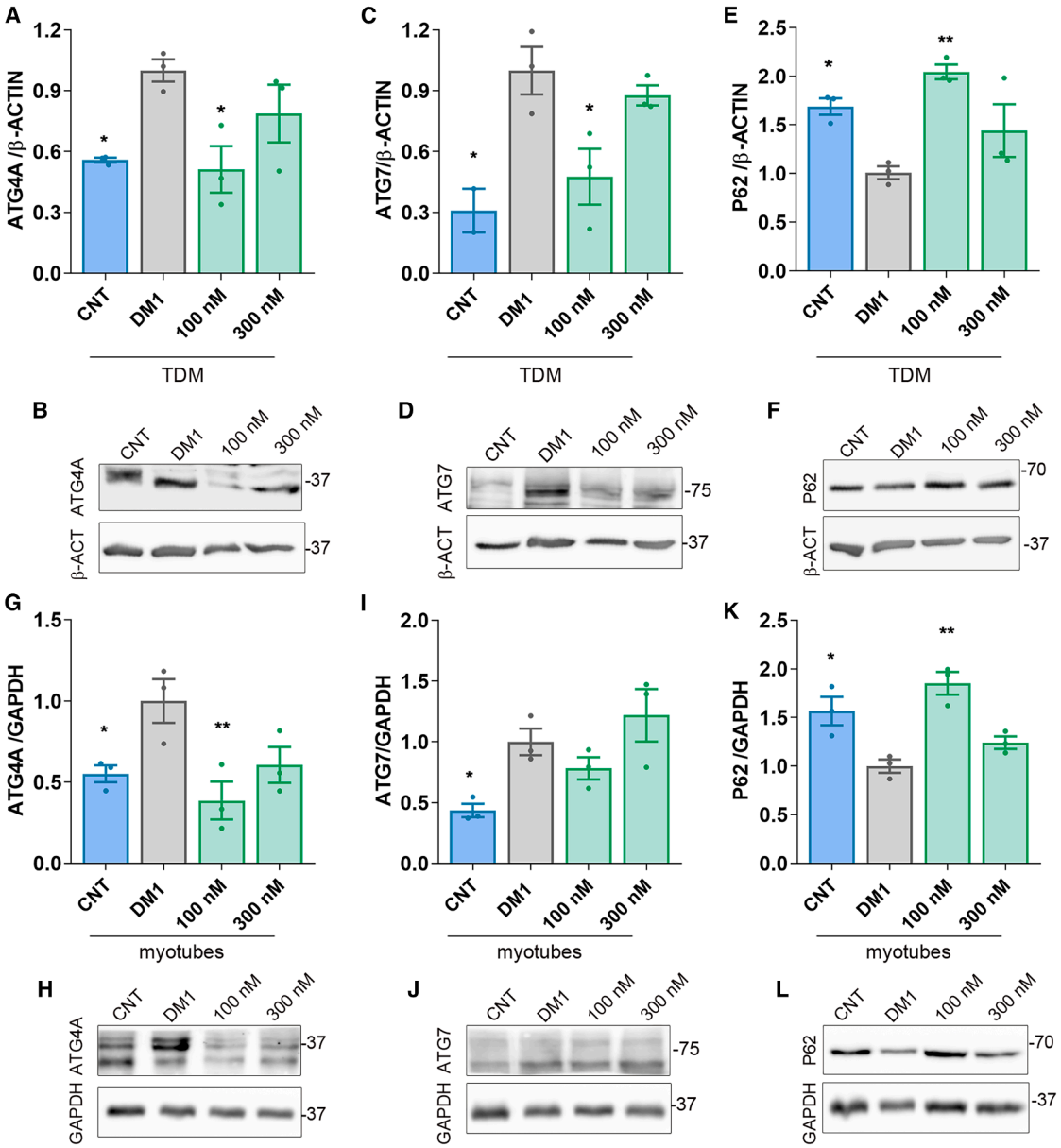

Figure 6. Replenishing miR-107 in DM1 cells restores autophagic pathway activity

Quantification (A, C, E, G, I, and K) and representative blots (B, D, F, H, J, and L) of immunoreactive bands with indication of molecular weight sizes to the right in kDa. ATG4A, ATG7, and P62 were immunodetected in control (CNT) and DM1 TDMs (A–F) or myotubes (G–L) untreated or treated with the indicated concentrations of agomiR-107 ($n = 3$) and differentiated for 7 days. Proteins were normalized to endogenous expression of β-ACT (A–F) or GAPDH (G–L). All comparisons were performed against untreated DM1 cells. The bar graphs show mean ± SEM. In all graphs, $^{*}p < 0.05$ and $^{**}p < 0.01$ according to one-way ANOVA test and Tukey's HSD post hoc test when necessary (A, C, E, G, I, and K).

capacity of cells and were assessed through immunofluorescent staining for the desmin protein, which provides crucial insights into the differentiation status of the affected cells[44,45] (Figures 8A and 8B).

In both TDMs and myotubes from patients, treatment with agomiR-107 notably increased the fusion index, with a 20%–40% rise in TDMs and a 10%–20% increase in myotubes (Figures 8C and 8D). Concurrently, the relative diameter of the myocytes increased significantly post-treatment. Analyzed diameter demonstrated that this phenotype recovered substantially upon agomiR supplement, exhibiting an around 2-fold increase in both muscular cell lines and at both tested concentrations of miRNA mimic (Figures 8E and 8F).

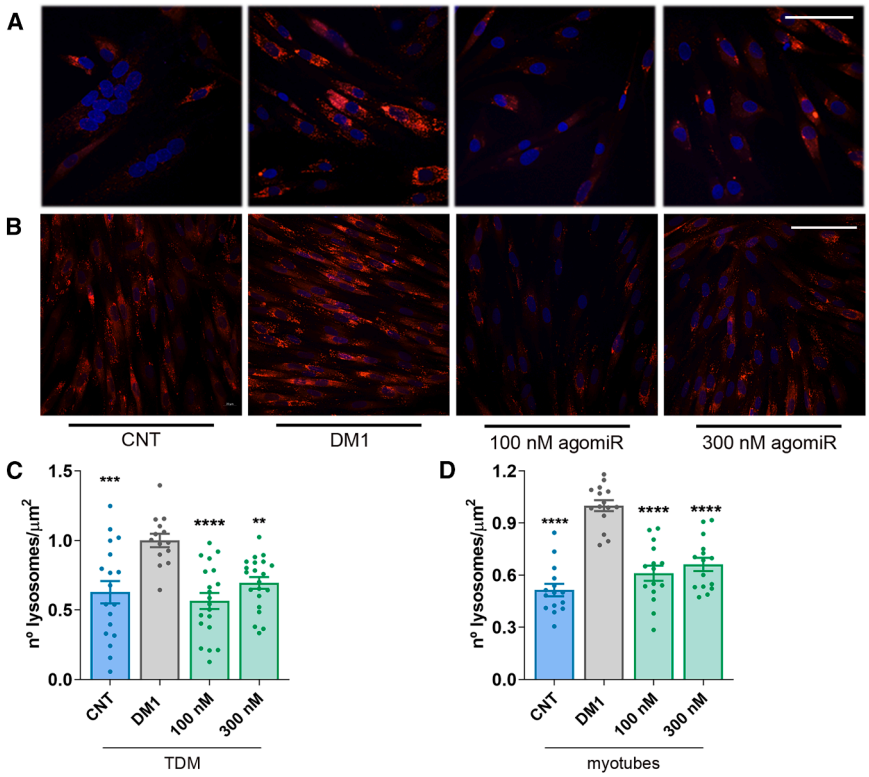

Figure 7. AgomiR-107 restores autophagic activity in DM1 cells

(A and B) Representative confocal images of LysoTracker staining (red) in CNT, untreated DM1 or DM1 supplemented with the indicated concentrations of miR-107 mimic in TDM (A) or myotubes (B). Nuclei were counterstained with DAPI. Scale bars, 100 µm. (C and D) Quantification of the number of lysosomes per μm^2 in each of the conditions described in A (C) or B (D) (between 14 and 22 images were analyzed per condition). All comparisons were performed against untreated DM1 cells. The bar graphs show mean ± SEM. In all graphs, $^{**}p < 0.01$, $^{***}p < 0.001$, and $^{****}p < 0.0001$ according to one-way ANOVA test and Tukey's HSD post hoc test when necessary (C and D).

The observed improvements in the fusion index and diameter following agomiR-107 treatment suggest a structural and functional rescue of the impaired differentiation phenotype in DM1 cellular models. The enhanced fusion index indicates improved myoblast fusion and myotube formation, which are critical for muscle development and regeneration. These findings align with our previous results, reinforcing the benefits of miR-107 modulation in counteracting key pathological features of DM1.

In conclusion, modulating miR-107 levels is a promising approach for intervention, showing potential to improve both the molecular and cellular aspects of DM1 pathology. These findings highlight the significance of miR-107 in DM1 and support further investigation into its applications in muscle and autophagy-related disorders.

DISCUSSION

The results presented in this study shed light on the intricate molecular mechanisms underlying DM1 pathogenesis, with a particular focus on miR-107 dysregulation. Our findings provide compelling evidence that the expanded CUG repeats in *DMPK* transcripts sequester miR-107 in the nucleus, impairing its function and resulting in dysregulation of its cytoplasmic targets, including *MSI2* and *DMPK*, which are repressed by this miRNA (Figure S8).

Previous studies have proposed the existence of miRNAs capable of binding to CUG repeats within the 3′ UTR of the *DMPK* gene. Computational analyses identified some miR-15b/16 family members, including miR-107, potentially binding to expanded CUG repeats contained in *DMPK*.[46,47] Our differential gene expression analysis revealed an imbalance in the regulation of miR-107 targets, with a significant upregulation of predicted targets in DM1 samples compared to controls. These data, together with those derived from DSF, FID and, EMSA assays, denoted that miR-107 is being retained by direct base-pairing in the nucleus with mutant *DMPK* transcripts, similar to the depletion observed over some RNA-binding proteins such as MBNLs[48] (Figure S8A). In this way, the deficit of miR-107 repressor activity in the cytoplasm, caused by its retention in the nucleus, may contribute to the disease's pathological hallmarks. These results are in line with others suggesting that miR-107 and miR-103 preferentially bind to mutant *DMPK* transcripts.[46] Indeed, miR-107 can be regarded as a competitor of MBNL1 for CUG binding, as revealed by the effect of miR-107 supplementation on nuclear RNA and MBNL1 foci. Given that MBNL1 has been shown to be required for RNA foci formation,[49] it is conceivable that mutant *DMPK* transcripts subsequently become translocated to the cytoplasm and are repressed by miR-107 or degraded by unidentified mechanisms (Figure S8B). Crucially, different concentrations of the mimetic have varying effects on the studied phenotypes, with results generally showing a greater capacity to reverse DM1-linked phenotypes when cells were treated with the lowest concentration (100 nM) of the mimetic. Based on the findings presented in Figure 4, where a broader range of concentrations was assessed, this effect might be due to the mimetic exhibiting a "bell-shaped" dose-response. In this type of response, a molecule or drug exerts its desired effect at low doses but loses efficacy at higher doses. This phenomenon could indicate that the optimal concentration range is crucial for achieving a corrective effect, as increasing the dose may counterintuitively reduce the mimetic's effectiveness.

Our results using a luciferase reporter system indicated that, in the cytoplasm, miR-107 regulates *DMPK* expression via RISC complexes according to the canonical mechanism of posttranscriptional

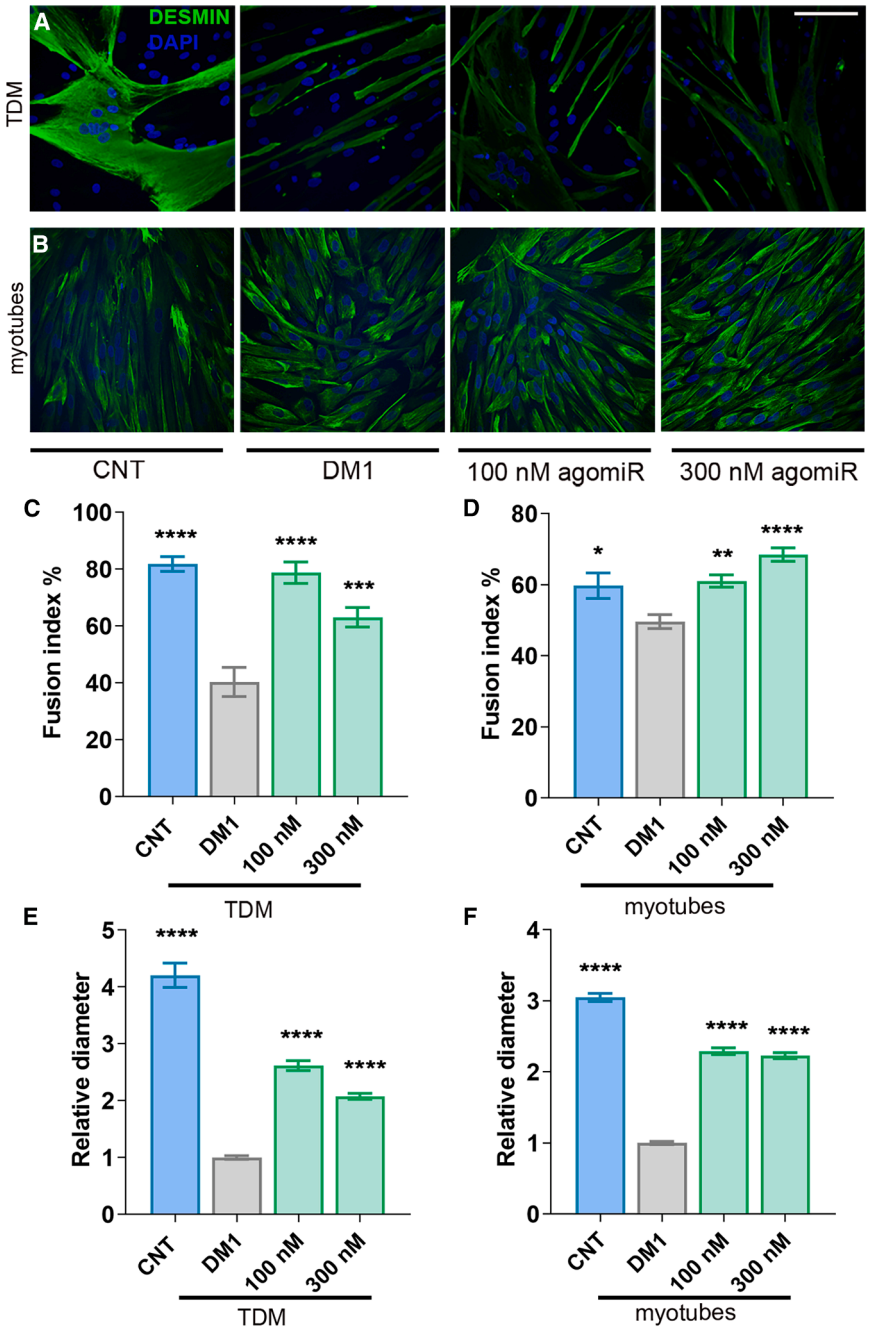

Figure 8. Replenishing miR-107 promotes muscle cell differentiation in DM1 cells

(A and B) Representative confocal microscopy images of immunofluorescence using an anti-desmin antibody (green) in CNT and DM1 TDM (A) or myotubes (B). The DM1 lines were treated with 100 or 300 nM agomiR-107 for 48 h. In all cases, cells were differentiated for 7 days. Nuclei were counterstained with DAPI. Scale bars, 100 μm. (C–F) Quantification of fusion index (C and D) and myotube diameter (E and F) in TDMs (C and E) and myotube (D and F). The bar graphs show mean ± SEM. $^{*}p < 0.05$, $^{**}p < 0.01$, $^{***}p < 0.001$, and $^{****}p < 0.0001$ according to one-way ANOVA test and Tukey's HSD post hoc test when necessary (C, D, E, and F).

regulation.[50] Moreover, this effect was observed on *DMPK* independently of the number of CUG repeats, demonstrating that *DMPK* is also a miR-107 target in non-pathological conditions (Figure S8B). Interestingly, when CTG repeats were removed from DMPK using the CRISPR-Cas9 technique, DMPK levels became unresponsive to miR-107 supplementation, unlike results in DM1 myotubes. This confirms that both binding (nucleus) and regulatory effects (cytoplasm) occur due to the base-pairing between miR-107 and CUG repeats reinforcing miR-107 as a negative regulator of DMPK expression and possibly an anti-DM1 molecule, as its presence in the nucleus releases key pathogenic hallmarks of DM1 such as MBNL1.

The overall function of mutant *DMPK* transcripts in the nucleus may be as miRNA sponges, sequestering miR-107 and potentially disrupting their regulatory functions in the cytoplasm. Given the established role of miRNAs in transcript regulation, their sequestration by *DMPK*, as exemplified by miR-107, may initiate a cascade of dysregulation within the pathways they govern. Restoring miR-107 levels through agomiR-107 shows potential in addressing the molecular and cellular abnormalities associated with DM1.

The consequences of miR-107 sequestration in DM1 extend beyond its direct interaction with *DMPK* transcripts, impacting downstream pathways implicated in muscle homeostasis. *In vivo* studies have shown decreased miR-107 expression after suspending mouse hind limbs for seven days and inducing muscle atrophy. In contrast, when mice were exposed to endurance exercise, miR-107 was upregulated, suggesting the involvement of this miRNA in muscle plasticity.[51] Similar results were reported by Safdar et al. in their study of miR-107 expression in quadriceps femoris from mice undergoing endurance exercise.[52] Reduced miR-107 availability leads to the derepression of its targets, including MSI2, whose upregulation in DM1 contributes to activating pro-atrophic pathways and exacerbates disease phenotypes.[29] Replenishment of miR-107 led to decreased expression of MSI2, with results in line with those previously obtained after silencing MSI2 with antisense oligonucleotides or inhibiting its activity by means of a small molecule.[30] Overall, we observed a reduction in the activity of the autophagic pathway toward levels observed in control cells.

It has previously been described that autophagy is hyperactive in DM1 and its deregulation contributes significantly to the loss of muscle homeostasis that ultimately induces the muscular atrophy characteristic of DM1. Moreover, restoring the activity of this catabolic pathway is sufficient to rescue pathological phenotypes of the disease linked to excessive protein degradation.[22,53] In addition, independent studies have recently demonstrated a negative correlation between increased autophagy markers and maximal isometric muscle strength[54] and even autophagy-related markers have been described as biomarkers of disease progression.[55] Given the involvement of excess autophagy in the imbalance of muscle homeostasis in DM1,[22,53,56] our results suggest that boosting miR-107 by a mimetic could be a promising therapeutic strategy for ameliorating muscle atrophy-related phenotypes in DM1 (Figure S8C).

miRNAs impact a wide range of biological processes, so the reduction and subcellular relocalization of miR-107 to the nucleus upon sequestration by mutant *DMPK* is expected to impact several pathways involved in DM1. Our findings add relevance to prior evidence of hyperactive autophagy processes in DM1. [21,57,58] In particular, these disruptions were ameliorated upon replenishing miR-107. This suggests that miR-107 sequestration increases muscle impairment, at least partly through the MSI2>miR-7 pathway, underscoring the potential benefit of targeting miR-107 in rescuing typical disease phenotypes, such as fusion index and myotube diameter, in DM1. However, our results suggest a decrease in miR-107 levels under DM1 conditions that could be contribute to the lack of miRNA function caused by its sequestration in CUG repeats. In recent years, it has become apparent that miRNA regulators are themselves subject to sophisticated control by a range of mechanisms, including miRNA gene transcription, miRNA processing, RNA editing of miRNAs, and regulation of miRNA function.[59] Specifically, the pri-mir-107 sequence is encoded within an intron of *PANK1* gene and the promoter regulating pri-mir-107 expression was found to be epigenetically regulated.[60] The pathological implications of epigenetics in DM1 are gaining more strength (Visconti et al. 2021). Thus, it cannot be ruled out that epigenetic defects could contribute to miR-107 downregulation.

Taken together, these observations and the results obtained in the current study suggest that miR-107 is involved in muscle maintenance. Hence, in DM1, miR-107 sequestration in RNA foci by expanded CUG might affect the DM1 landscape. By elucidating the interaction between miR-107 and expanded CUG repeats in *DMPK* transcripts, we shed light on a novel aspect of DM1 pathogenesis. These findings underscore the potential of targeting miR-107 and its downstream pathways, offering new avenues for developing targeted therapies for DM1.

MATERIALS AND METHODS

miR-107 targets analyses

Available transcriptomics analyses of immortalized control and DM1 TDMs[35] at 4 and 8 days of differentiation[23,61] were reanalyzed (n = 3 in each condition). The data were deposited in the Gene Expression Omnibus database (accession nos. GSE173359 and GSE128844). Differential gene expression (DEG) analysis was performed using the edge R package with the thresholds of a $\log_2$ fold change of 0 and an adjusted p value under 0.05. Next, we searched for potential hsa-miR-107 targets in the DEG results using the gene-target database mirTarbase.[32,33] A similar DEG and miR-107 target analysis was performed in control and DM1 patients' tibialis biopsy RNA-seq data available at DMseq.org,[34] with the same cut off points as used for the cell culture (n = 5 for controls and 22 for DM1 samples).

Cell culture and transfection

TDM and immortalized myoblast were obtained from the Institute of Myology, Paris.[35] Cells were cultured as previously described.[21,35] Three different immortalized CRISPR-edited myoblast lines (derived from the DM1 immortalized myoblast) were also used: 4F9 (2,600 CTG) as CRISPR control, 3B1Δ/Δ, and 4A3Δ/Δ, with CTG deletion in both alleles.[40] Cells were transfected after 4 days in differentiation medium (MDM) with agomiR-107 using Lipofectamine RNAiMAX transfection reagent (Invitrogen; Madrid, Spain) following the manufacturer's recommendations, to final concentrations ranging from 0.25 to 1,000 nM depending on the experiment. After 48 h, the medium containing the agomiR was replaced by fresh MDM. HEK 293T cells were cultured as described in a study by Koscianska et al.[18]

Oligonucleotides

The oligonucleotides used were as follows:

miR-107 sense strand: 5′-AGCAGCAUUGUACAGGGCUAUCA-3′

miR-107 antisense strand:

5′-$_{m}$U*$_{m}$G*$_{m}$A$_{m}$U$_{m}$A$_{m}$G$_{m}$C$_{m}$C$_{m}$C$_{m}$U$_{m}$G$_{m}$U$_{m}$A$_{m}$C$_{m}$A$_{m}$A$_{m}$U$_{m}$G$_{m}$C$_{m}$U*$_{m}$G*$_{m}$C*$_{m}$U*-3′-chol.where "m" denotes 2′-Ome RNA, * denotes phosphorothioate internucleoside linkages, and "chol" denotes a cholesterol group.

The two strands were hybridized by mixing them in equal concentrations. The mix was heated to 95°C for 2 min and slowly cooled to room temperature.

Control RNA (cRNA) for EMSA assay was as follows:

5′-UUCUCCGAACUUCUGACUUUG-3′ (cRNA).

The oligonucleotides were synthesized by Biomers (Ulm, Germany).

Cell fraction, miRNA isolation, and RNA-seq bioinformatics analysis

Immortalized DM1 and CNT myoblast[35] (n = 5) differentiated for 5–8 days were harvested for RNA isolation, and were fractioned into nucleus and cytoplasms using a PARIS kit (Invitrogen) until the sub-cellular fraction separation step, followed by miRNA isolation using miRNeasy Mini Kit (QIAGEN; Hilden, Germany).

miRNA-enriched RNA was sent to the Oxford Genomics Centre for sequencing. For miRNA sequencing, cDNA libraries were prepared using a TruSeq Small RNA Library Preparation Kit (Illumina) following the manufacturer's instructions. Sequencing was performed using rapid mode in a HiSeq 2500 System (Illumina).

Total RNA was ribodepleted and this fraction converted to cDNA. A second strand cDNA synthesis incorporated dUTP. Next, the cDNA was end-repaired, A-tailed, and adapter-ligated. Prior to amplification, samples underwent uridine digestion, and prepared libraries were size-selected, multiplexed, and quality-checked before sequencing. Pair-end sequencing was performed in a HiSeq 4000 System (Illumina).

Single-end reads from the miRNA library were cleaned from adaptors using Trimmomatic,[62] and quality was checked with the FastQC application to remove reads with low-quality values from the dataset (Phred score threshold below 20). Follow-up analyses were computed using the webserver sRNAtoolbox (Aparicio-Puerta et al., 2022), including reads assembling, reads mapping on human GRCh38_p12 reference genome, reads annotation based on miRBase reference database, and reads count. Differential expression analyses were carried out in DEseq2. These data have been deposited in the Gene Expression Omnibus (GEO) database (accession no. GSE262164).

Toxicity assay

DM1 TDMs were seeded in 96-well plates with 1.0×10^4 cells per well. Cells were transfected with increasing agomiR-107 concentrations (from 1 nM to 1 μM) per quadruplicate. To measure cell viability, 20 μL of (3-(4,5-dimethylthiazol-2-yl)-5-(3-carboxymethoxyphenyl)-2-(4-sulfophenyl)-2H-tetrazolium inner salt)/phenazine methosulfate (MTS/PMS;CellTiter 96 AQueous Non-Radioactive Cell Proliferation Assay, Promega; Madison, WI, USA) was added to each well after 7 days of differentiation. The mix contained 100 μL of MDM and was incubated for 4 h at 37°C in a humidified chamber with 5% CO_2. Absorbance at 490 nm was measured using an Infinite 200 PRO plate reader (Tecan Life Sciences; Männedorf, Switzerland). Data were transformed to a survival percentage relative to cells not exposed to agomiR, which was considered 100% viability. TC_{50} was obtained using the least-squares non-linear regression model.

Luciferase reporter assay

HEK293 cells were seeded at 60,000 cells per well in p24 plates. After 24 h, cells were transfected with 0.5 μg/mL of the pmiR-GLO plasmid containing varying CTG repeat numbers (0, 5, 44, 53, and 72) and agomiR at a concentration of 100 nM. Additionally, to eliminate CTG repeats and establish a negative control, the pmiR-GLO plasmid with 72 CUG repeats was digested with *Dra*I and *Xba*I restriction enzymes and subsequently purified. Cells were harvested at 72 and 96 h following the Dual-Luciferase Reporter Assay System protocol (E1960, Promega). Luciferase activity was measured using a plate reader (Tecan 200 Infinity Pro) with technical quadruplicates. Analysis was performed by normalizing firefly luciferase activity to *Renilla* luciferase.

EMSA

The mixtures of RNA (CUG_{20}) and miR-107 or cRNA in different ratios in Tris buffer (Tris 10 mM, NaCl 100 mM [pH 7.4]) were incubated for 1 h at room temperature (RT) and loaded onto a native 16% polyacrylamide mini-gel in 1× TBE. The gels were run for 90 min at 120 V and stained with Sybr Green (1:100). The bands were displayed and quantified with a G800 BIORAD densitometer and analysis software. The concentration of CUG_{20} was confirmed by UV-Vis, considering the extinction coefficient provided by the manufacturer. Prior to the experiments, CUG_{20} RNA was denatured at 95°C for 10 min and left to cool to room temperature overnight to form secondary structures.

Fluorescence emission titrations

A solution of 0.25 μM thiazole orange in 10 mM sodium cacodylate buffer (pH 7.4) was titrated with the CUG_{20} until saturation of fluorescence emission. Onto a mixture of prefolded 2 μM and 0.25 μM CUG_{20}-hairpin, addition of increasing amounts of agomiR-107 or cRNA (ranging from 0.25 to 20 equivalents) was followed by a 2 min equilibration period before the fluorescence spectrum was recorded. The emission spectra were recorded between 505 and 800 nm with an excitation wavelength of 495 nm in 1 cm path-length quartz cuvette. The emission spectra were recorded on a PTI Spectrometer. Spectra were smoothed using the Savitzky-Golay algorithm and emission maxima were fitted using non-linear methods.

RNA isolation and RT-qPCR

We seeded 1×10^6 cells per replicate in Petri plates. RNA was isolated using the miRNeasy mini kit (QIAGEN) according to the manufacturer's instructions. RNA (1 μg) was digested with DNase I (Invitrogen) and reverse-transcribed with SuperScript II (Invitrogen) using random hexanucleotides. RT-qPCR was performed using 5× HOT FIREPol EvaGreen qPCR mix plus (ROX) (Solis BioDyne) and the following primers (5′-to-3: GAPDH (fwd CATCTTCCAGGAGCGAGATC; rev GTTCACACCCATGACGAACAT), GPI (fwd CAGGGCATCATCTGGGACAT; rev TCTTAGCCAGCTGCTTTCCC), and MSI2 (fwd GCAGACCTCACCAGATAGCCTT; rev AAGCCTCTGGAGCGTTTCGTAG). *DMPK* (FAM-labeled probe) quantification was normalized by *GAPDH* (MAX-labeled probes). The sequence of primers and probe (acquired from Integrated DNA Technologies; Leuven, Belgium) for *DMPK* quantification were as follows: fwd AGCCTGAGCCGGGAGATG, rev GCGTAGTTGACTGGCGAAGTT, and probe AGGCCATCCGCACGGACAACC; and primers for *GAPDH* were as follows: fwd CAACGGATTTGGTCGTATTGG, rev TGATGGCAACAATATCCACTTTACC, and probe CGCCTGGTCACCAGGGCTGCT. miR-7 and miR-107 expression was quantified using specific miRCURY™-locked nucleic acid microRNA PCR primers (Exiqon). Relative gene expression was normalized to *U1* or *U6* small nuclear RNAs (snRNAs). mRNA and miRNA levels were assessed with Applied Biosystems QuantStudio 5 and 3 Real-Time PCR System, and quantified using the delta-delta Ct method ($2^{-\Delta\Delta Ct}$).

Western blot

To extract total protein, 1×10^6 cells were sonicated in radioimmunoprecipitation assay (RIPA) buffer supplemented with protease and phosphatase inhibitor cocktails (Roche Applied Science). The total protein content was quantified spectrophotometrically at 562 nm using the Pierce BCA protein assay kit (Thermo Fisher Scientific; Grand Island, NY, USA) with bovine serum albumin (BSA) as the protein standard. Subsequently, 20–30 μg of protein samples underwent denaturation at 100°C for 5 min, followed by electrophoresis on 12% SDS-PAGE gels and transfer onto 0.45 μm nitrocellulose membranes (GE Healthcare). All the primary antibodies were used with 5% non-fat dried milk in PBS-T (PBS 1× containing 0.05% Tween 20) as blocking buffer except for ATG7 which needs to be blocked with 5% BSA in PBS-T (PBS 1× containing 0.05% Tween 20). The antibodies comprised rabbit anti-ATG4A (1:1,000, D62C10, Cell Signaling Technology; Danvers, MA, USA), rabbit anti-MSI2 antibody (1:1,000, EP1305Y; Abcam; Cambridge, UK), rabbit anti-ATG7 (1:1,000, D12B11, Cell Signaling Technology), mouse anti-SQSTM1 (1:1,000, 2C11 Abcam), and mouse anti-DMPK (1:200, MANDM5 5G12; Developmental Studies Hybridoma Bank (DSHB)). Membrane blocking was performed by immersion in a solution of 5% non-fat dried milk in PBS-T (0.05% Tween 20) for 1 h, except for the ATG7 antibody, which underwent incubation in 5% BSA. The membranes were incubated overnight at 4°C in a 5% blocking solution containing primary antibodies at appropriate dilutions. Immunoreactive bands were visualization using the Signal West Pico PLUS Chemiluminescent Substrate (Thermo Fisher Scientific), and subsequent imaging was performed using an Amersham ImageQuant 800 system (GE Healthcare; Pittsburgh, PA, USA). Quantitative analysis of the obtained images was conducted using ImageJ (NIH) software.

DSF

For DSF analysis,[63] we utilized the StepOnePlus Real-Time PCR (Life Technologies) along with melting curve software, with a sample volume of 50 μL for each run. In this experiment, we incorporated the RiboGreen dye at a final concentration of 300 nM. Additionally, we employed synthetic double-stranded CUG RNA (CUG_{20}) and CGA RNA (CGA_{20}) as an unstructured control, both acquired at IDT (Integrated DNA Technologies) and used at a final concentration of 600 nM. To maintain the integrity of the RNA we used a sodium cacodylate buffer with a pH of 6.5. The study encompassed 17 concentrations (ranging from 0.25 nM to 1 μM) of the miR-107 sense strand with technical triplicates.

Ribonuclear foci and MBNL1 detection

Fibroblasts were seeded into 96- and 24-well plates and after agomiR-107 treatment, cells were fixed in 4% PFA for 15 min at RT followed by washing in 1× PBS. Foci detection was performed as described in a study by Sabater-Arcis et al.[21] using an IN-cell analyzer 2200 imaging system. *In situ* detection of CUG repeats and MBNL1 immunofluorescence was performed in 24-well plates. A permeabilization step with PBS-T (0.3% Triton X-100) was followed by a blocking step for 30 min using a blocking buffer composed of PBS-T supplemented with 1% normal goat serum. Anti-MBNL1 antibody (1:100, MB1a(4A8), DSHB) was incubated overnight at 4°C followed by three washes with PBS-T 1 × 0.3% Triton. A highly cross-absorbed anti-mouse secondary antibody Alexa Fluor Plus 488 (Thermo Fisher Scientific) was then applied at a dilution of 1:100 and incubated for 1.5 h at RT. Cells were washed with SSC UltraPure buffer diluted 2× (Thermo Fisher Scientific) supplemented with 30% formamide for 10 min at RT. Subsequently, Cy3-(CAG)7-Cy3 labeled probe, diluted at 1:100, was added to cells in hybridization buffer (8 mL formamide, 2 mL SSC UltraPure 20×, 4 mL BSA 1% in PBS, 2 g dextran sulfate, 2 mL tRNA [10 mg/mL], 2 mL vanadyl complex, 2 mL herring sperm) and incubated in a humid chamber at 37°C for 2 h. Afterward, a double wash was performed with 2× dilution of SSC UltraPure (Thermo Fisher Scientific) with 30% formamide at 45°C for 15 min each, followed by a triple wash with filtered PBS 1× for 10 min each at RT. Finally, samples were mounted using VECTASHIELD medium containing DAPI (Vector Laboratories; London, UK) and imaged in an LSM 800 confocal microscope (Zeiss; Jena, Germany). MBNL1 and foci colocalization were quantified using ZEN, the Zeiss software analysis tool.

Immunofluorescence methods

To carry out DESMIN immunodetection, TDMs and immortalized myoblast were seeded in 24-well plates, treated with agomiR-107, and differentiated for 7 days. Cells were fixed with 4% PFA for 15 min at RT and were processed using mouse anti-DESMIN (1:50, D33, Abcam), biotin-conjugated anti-mouse-IgG (1:200, Sigma-Aldrich, St. Louis, MO, USA) and streptavidin-FITC (1:200, Vector). Images were taken with an LSM800 confocal microscope (Zeiss). The fusion index was defined as the percentage of nuclei within myotubes (>2 myonuclei) out of the total number of nuclei in each condition. Myotube diameters were measured at 5 points along the entire tube. Quantification was performed using ImageJ software (NIH).

For LysoTracker staining, a 24-well plate was seeded, and miR-107 mimic (100 and 300 μM) was used to treat cells. Samples were incubated with 100 nM LysoTracker RED-DND99 (Invitrogen) at 37°C for 30 min. After two washes with warmed PBS, cells were fixed with 4% PFA for 15 min, followed by additional washes in 1× PBS. Subsequently, cells were mounted using Vectashield (Vector Laboratories) containing 2 μg/mL DAPI. Micrographs were acquired using an LSM800 confocal microscope (Zeiss).

Lysotracker signal quantification

Quantification was performed by analyzing 15 micrographs per condition using ImageJ software (Fiji).[64] A custom macro was developed to automate image processing and data extraction. Confocal microscopy images were acquired in two channels: red, corresponding to LysoTracker signal, and blue, corresponding to DAPI staining for nuclei. Only the red channel was used for LysoTracker signal quantification.

The analysis procedure involved several steps: (1) opening and splitting the channels to select the red one; (2) converting the image to

8-bit and applying preprocessing steps, including filtering to enhance particle definition and background noise subtraction; and (3) segmenting particles using automatic thresholding. The Analyze Particles function in ImageJ was then used to quantify particle count. Additionally, the total myotube area in each image was measured to normalize the data, reported as particle density per unit area (μm^2).

Statistical analyses

In all molecular studies, for comparison of mean data, all parameters were assumed to follow a normal distribution. Experiments with two conditions were compared using Student's t test ($\alpha = 0.05$), applying Welch's correction when necessary. For comparisons of more conditions, one-way ANOVA ($\alpha = 0.05$), and Tukey's honest significant difference (HSD) post hoc test were employed when necessary. Two-way ANOVA ($\alpha = 0.05$) was used to compare the differences when there were two variables, followed by Tukey's multiple comparison test.

DATA AVAILABILITY

This study includes data deposited in public external repositories. Additional data are available in the article and/or additional files and via corresponding authors upon reasonable request.

ACKNOWLEDGMENTS

The MB1a(4A8) and MANDM5 5G12 antibodies (developed by Morris, G.E of Wolfson Centre for Inherited Neuromuscular Disease, RJAH Orthopaedic Hospital) were obtained from the Developmental Studies Hybridoma Bank, created by the Eunice Kennedy Shriver National Institute of Child Health and Human Development (NICHD) of the NIH and maintained at The University of Iowa, Department of Biology, Iowa City, IA 52242.

The authors thank the Department of Molecular and Systems Biology of the Institute of Bioorganic Chemistry at the Polish Academy of Sciences[18] for kindly supplying the plasmids utilized in this study for luciferase assays.

This study has been funded by Instituto de Salud Carlos III (ISCIII) through the project PI21/00311 and co-funded by the European Union (ERDF funds) to A.B., and PROMETEO/2020/081 and CIPROM/2023/22 from the Generalitat Valenciana to R.A. M.S.-A. is grateful for the support of the Margarita Salas postdoctoral research grant (MS21-143). N.M. was supported by a predoctoral fellowship (PRE2019-090622) from the Ministerio de Ciencia e Innovación-Agencia Estatal de Investigación. A.B. is grateful for the support of the Instituto de Salud Carlos III, Ministerio de Ciencia, Innovación y Universidades, as a Miguel Servet postdoctoral grantee (CP24/00016). Part of the equipment employed in this work has been funded by Generalitat Valenciana and co-financed with ERDF funds (OP ERDF of Comunitat Valenciana 2014-2020).

AUTHOR CONTRIBUTIONS

R.A. provided the conceptual framework for the study. R.A., A.B., T.S., and M.P.A. conceived and supervised the experiments. R.A., M.P.A., and A.B. administered the project. R.A., A.B., and M.P.A. obtained funds. N.M. and M.S.-A. performed the experiments and analyzed data. J.O. provided the immortalized myoblasts. J.E.-E. analyzed miR-107 targets. D.S.-M., M.A.V., and M.J.A.W. provided nuclear and cytosolic miRNA data. L. M.-R., E.G.-E., and J.G.-G. designed, performed, and analyzed EMSA assays. N.M. wrote the original article. R.A. and A.B. participated in the review and editing of the manuscript.

DECLARATION OF INTERESTS

The authors declare no competing interests.

SUPPLEMENTAL INFORMATION

Supplemental information can be found online at https://doi.org/10.1016/j.omtn.2025.102584.

REFERENCES

1. André, L.M., Ausems, C.R.M., Wansink, D.G., and Wieringa, B. (2018). Abnormalities in Skeletal Muscle Myogenesis, Growth, and Regeneration in Myotonic Dystrophy. Front. Neurol. *9*, 368. https://doi.org/10.3389/FNEUR.2018.00368.

2. Hamel, J.I. (2022). Myotonic Dystrophy. Continuum *28*, 1715–1734. https://doi.org/10.1212/CON.0000000000001184.

3. Rosado Bartolomé, A., Puertas Martín, V., Domínguez González, C., and Ramos Miranda, M. (2022). [Cognitive impairment in myotonic dystrophy type 1 (Steinert's disease)]. SEMERGEN, Soc. Esp. Med. Rural Generalista *48*, 208–213. https://doi.org/10.1016/J.SEMERG.2022.01.013.

4. Brook, J.D., McCurrach, M.E., Harley, H.G., Buckler, A.J., Church, D., Aburatani, H., Hunter, K., Stanton, V.P., Thirion, J.P., Hudson, T., et al. (1992). Molecular basis of myotonic dystrophy: expansion of a trinucleotide (CTG) repeat at the 3' end of a transcript encoding a protein kinase family member. Cell *68*, 799–808. https://doi.org/10.1016/0092-8674(92)90154-5.

5. Taylor, K., Sznajder, L.J., Cywoniuk, P., Thomas, J.D., Swanson, M.S., and Sobczak, K. (2018). MBNL splicing activity depends on RNA binding site structural context. Nucleic Acids Res. *46*, 9119–9133. https://doi.org/10.1093/NAR/GKY565.

6. Holt, I., Jacquemin, V., Fardaei, M., Sewry, C.A., Butler-Browne, G.S., Furling, D., Brook, J.D., and Morris, G.E. (2009). Muscleblind-like proteins: similarities and differences in normal and myotonic dystrophy muscle. Am. J. Pathol. *174*, 216–227. https://doi.org/10.2353/AJPATH.2009.080520.

7. Cox, D.C., Guan, X., Xia, Z., and Cooper, T.A. (2020). Increased nuclear but not cytoplasmic activities of CELF1 protein leads to muscle wasting. Hum. Mol. Genet. *29*, 1729–1744. https://doi.org/10.1093/hmg/ddaa095.

8. Holt, I., Mittal, S., Furling, D., Butler-Browne, G.S., Brook, J.D., and Morris, G.E. (2007). Defective mRNA in myotonic dystrophy accumulates at the periphery of nuclear splicing speckles. Genes Cells *12*, 1035–1048. https://doi.org/10.1111/J.1365-2443.2007.01112.X.

9. Konieczny, P., Stepniak-Konieczna, E., and Sobczak, K. (2014). MBNL proteins and their target RNAs, interaction and splicing regulation. Nucleic Acids Res. *42*, 10873–10887. https://doi.org/10.1093/NAR/GKU767.

10. Chau, A., and Kalsotra, A. (2015). Developmental insights into the pathology of and therapeutic strategies for DM1: Back to the basics. Dev. Dyn. *244*, 377–390. https://doi.org/10.1002/DVDY.24240.

11. Ozimski, L.L., Sabater-Arcis, M., Bargiela, A., and Artero, R. (2021). The hallmarks of myotonic dystrophy type 1 muscle dysfunction. Biol. Rev. Camb. Philos. Soc. *96*, 716–730. https://doi.org/10.1111/BRV.12674.

12. Saliminejad, K., Khorram Khorshid, H.R., Soleymani Fard, S., and Ghaffari, S.H. (2019). An overview of microRNAs: Biology, functions, therapeutics, and analysis methods. J. Cell. Physiol. *234*, 5451–5465. https://doi.org/10.1002/JCP.27486.

13. O'Brien, J., Hayder, H., Zayed, Y., and Peng, C. (2018). Overview of MicroRNA Biogenesis, Mechanisms of Actions, and Circulation. Front. Endocrinol. *9*, 402. https://doi.org/10.3389/FENDO.2018.00402.

14. Cerro-Herreros, E., González-Martínez, I., Moreno, N., Espinosa-Espinosa, J., Fernández-Costa, J.M., Colom-Rodrigo, A., Overby, S.J., Seoane-Miraz, D., Poyatos-García, J., Vilchez, J.J., et al. (2021). Preclinical characterization of antagomiR-218 as a potential treatment for myotonic dystrophy. Mol. Ther. Nucleic Acids *26*, 174–191. https://doi.org/10.1016/J.OMTN.2021.07.017.

15. Cerro-Herreros, E., Sabater-Arcis, M., Fernandez-Costa, J.M., Moreno, N., Perez-Alonso, M., Llamusi, B., and Artero, R. (2018). miR-23b and miR-218 silencing increase Muscleblind-like expression and alleviate myotonic dystrophy phenotypes in mammalian models. Nat. Commun. *9*, 2482. https://doi.org/10.1038/s41467-018-04892-4.

16. Cerro-Herreros, E., González-Martínez, I., Moreno-Cervera, N., Overby, S., Pérez-Alonso, M., Llamusí, B., and Artero, R. (2020). Therapeutic Potential of AntagomiR-23b for Treating Myotonic Dystrophy. Mol. Ther. Nucleic Acids *21*, 837–849. https://doi.org/10.1016/j.omtn.2020.07.021.

17. Dong, W., Chen, X., Wang, M., Zheng, Z., Zhang, X., Xiao, Q., and Peng, X. (2019). Mir-206 partially rescues myogenesis deficiency by inhibiting CUGBP1 accumulation in the cell models of myotonic dystrophy. Neurol. Res. *41*, 9–18. https://doi.org/10.1080/01616412.2018.1493963.

18. Koscianska, E., Witkos, T.M., Kozlowska, E., Wojciechowska, M., and Krzyzosiak, W.J. (2015). Cooperation meets competition in microRNA-mediated DMPK transcript regulation. Nucleic Acids Res. *43*, 9500–9518. https://doi.org/10.1093/NAR/GKV849.

19. Shen, X., Xu, F., Li, M., Wu, S., Zhang, J., Wang, A., Xu, L., Liu, Y., and Zhu, G. (2020). miR-322/-503 rescues myoblast defects in myotonic dystrophy type 1 cell model by targeting CUG repeats. Cell Death Dis. *11*, 891. https://doi.org/10.1038/s41419-020-03112-6.

20. Franco-Romero, A., and Sandri, M. (2021). Role of autophagy in muscle disease. Mol. Aspects Med. *82*, 101041. https://doi.org/10.1016/J.MAM.2021.101041.

21. Sabater-Arcis, M., Bargiela, A., Furling, D., and Artero, R. (2020). miR-7 Restores Phenotypes in Myotonic Dystrophy Muscle Cells by Repressing Hyperactivated Autophagy. Mol. Ther. Nucleic Acids *19*, 278–292. https://doi.org/10.1016/J.OMTN.2019.11.012.

22. Bargiela, A., Cerro-Herreros, E., Fernandez-Costa, J.M., Vilchez, J.J., Llamusi, B., and Artero, R. (2015). Increased autophagy and apoptosis contribute to muscle atrophy in a myotonic dystrophy type 1 Drosophila model. Dis. Model. Mech. *8*, 679–690. https://doi.org/10.1242/DMM.018127.

23. Bargiela, A., Sabater-Arcis, M., Espinosa-Espinosa, J., Zulaica, M., Lopez de Munain, A., and Artero, R. (2019). Increased Muscleblind levels by chloroquine treatment improve myotonic dystrophy type 1 phenotypes in in vitro and in vivo models. Proc. Natl. Acad. Sci. USA *116*, 25203–25213. https://doi.org/10.1073/PNAS.1820297116.

24. Gu, D.N., Jiang, M.J., Mei, Z., Dai, J.J., Dai, C.Y., Fang, C., and Huang, Q. (2017). microRNA-7 impairs autophagy-derived pools of glucose to suppress pancreatic cancer progression. Cancer Lett. *400*, 69–78. https://doi.org/10.1016/J.CANLET.2017.04.020.

25. Choudhury, N.R., de Lima Alves, F., de Andrés-Aguayo, L., Graf, T., Cáceres, J.F., Rappsilber, J., and Michlewski, G. (2013). Tissue-specific control of brain-enriched miR-7 biogenesis. Genes Dev. *27*, 24–38. https://doi.org/10.1101/GAD.199190.112.

26. Kumar, S., Downie Ruiz Velasco, A., and Michlewski, G. (2017). Oleic Acid Induces MiR-7 Processing through Remodeling of Pri-MiR-7/Protein Complex. J. Mol. Biol. *429*, 1638–1649. https://doi.org/10.1016/J.JMB.2017.05.001.

27. Matalkah, F., Jeong, B., Sheridan, M., Horstick, E., Ramamurthy, V., and Stoilov, P. (2022). The Musashi proteins direct post-transcriptional control of protein expression and alternate exon splicing in vertebrate photoreceptors. Commun. Biol. *5*, 1011. https://doi.org/10.1038/S42003-022-03990-W.

28. Cragle, C.E., MacNicol, M.C., Byrum, S.D., Hardy, L.L., Mackintosh, S.G., Richardson, W.A., Gray, N.K., Childs, G.V., Tackett, A.J., and MacNicol, A.M. (2019). Musashi interaction with poly(A)-binding protein is required for activation of target mRNA translation. J. Biol. Chem. *294*, 10969–10986. https://doi.org/10.1074/JBC.RA119.007220.

29. Sabater-Arcis, M., Moreno, N., Sevilla, T., Perez Alonso, M., Bargiela, A., and Artero, R. (2024). Msi2 enhances muscle dysfunction in a myotonic dystrophy type 1 mouse model. Biomed. J. *47*, 100667. https://doi.org/10.1016/J.BJ.2023.100667.

30. Sabater-Arcis, M., Bargiela, A., Moreno, N., Poyatos-Garcia, J., Vilchez, J.J., and Artero, R. (2021). Musashi-2 contributes to myotonic dystrophy muscle dysfunction by promoting excessive autophagy through miR-7 biogenesis repression. Mol. Ther. Nucleic Acids *25*, 652–667. https://doi.org/10.1016/J.OMTN.2021.08.010.

31. Dong, P., Xiong, Y., Hanley, S.J.B., Yue, J., and Watari, H. (2017). Musashi-2, a novel oncoprotein promoting cervical cancer cell growth and invasion, is negatively regulated by p53-induced miR-143 and miR-107 activation. J. Exp. Clin. Cancer Res. *36*, 150. https://doi.org/10.1186/S13046-017-0617-Y.

32. Hsu, S.D., Lin, F.M., Wu, W.Y., Liang, C., Huang, W.C., Chan, W.L., Tsai, W.T., Chen, G.Z., Lee, C.J., Chiu, C.M., et al. (2011). miRTarBase: a database curates experimentally validated microRNA-target interactions. Nucleic Acids Res. *39*, D163–D169. https://doi.org/10.1093/NAR/GKQ1107.

33. Huang, H.Y., Lin, Y.C.D., Cui, S., Huang, Y., Tang, Y., Xu, J., Bao, J., Li, Y., Wen, J., Zuo, H., et al. (2022). miRTarBase update 2022: an informative resource for experimentally validated miRNA–target interactions. Nucleic Acids Res. *50*, D222–D230. https://doi.org/10.1093/NAR/GKAB1079.

34. Wang, E.T., Treacy, D., Eichinger, K., Struck, A., Estabrook, J., Olafson, H., Wang, T. T., Bhatt, K., Westbrook, T., Sedehizadeh, S., et al. (2019). Transcriptome alterations in myotonic dystrophy skeletal muscle and heart. Hum. Mol. Genet. *28*, 1312–1321. https://doi.org/10.1093/HMG/DDY432.

35. Arandel, L., Polay Espinoza, M., Matloka, M., Bazinet, A., De Dea Diniz, D., Naouar, N., Rau, F., Jollet, A., Edom-Vovard, F., Mamchaoui, K., et al. (2017). Immortalized human myotonic dystrophy muscle cell lines to assess therapeutic compounds. Dis. Model. Mech. *10*, 487–497. https://doi.org/10.1242/dmm.027367.

36. de Rie, D., Abugessaisa, I., Alam, T., Arner, E., Arner, P., Ashoor, H., Åström, G., Babina, M., Bertin, N., Burroughs, A.M., et al. (2017). An integrated expression atlas of miRNAs and their promoters in human and mouse. Nat. Biotechnol. *35*, 872–878. https://doi.org/10.1038/nbt.3947.

37. Galka-Marciniak, P., Urbanek, M.O., and Krzyzosiak, W.J. (2012). Triplet repeats in transcripts: structural insights into RNA toxicity. Biol. Chem. *393*, 1299–1315. https://doi.org/10.1515/hsz-2012-0218.

38. Wicks, S.L., and Hargrove, A.E. (2019). Fluorescent indicator displacement assays to identify and characterize small molecule interactions with RNA. Methods *167*, 3–14. https://doi.org/10.1016/j.ymeth.2019.04.018.

39. Tran, P.L.T., Largy, E., Hamon, F., Teulade-Fichou, M.-P., and Mergny, J.-L. (2011). Fluorescence intercalator displacement assay for screening G4 ligands towards a variety of G-quadruplex structures. Biochimie *93*, 1288–1296. https://doi.org/10.1016/j.biochi.2011.05.011.

40. van Agtmaal, E.L., André, L.M., Willemse, M., Cumming, S.A., van Kessel, I.D.G., van den Broek, W.J.A.A., Gourdon, G., Furling, D., Mouly, V., Monckton, D.G., et al. (2017). CRISPR/Cas9-Induced (CTG·CAG)n Repeat Instability in the Myotonic Dystrophy Type 1 Locus: Implications for Therapeutic Genome Editing. Mol. Ther. *25*, 24–43. https://doi.org/10.1016/J.YMTHE.2016.10.014.

41. Ketley, A., Chen, C.Z., Li, X., Arya, S., Robinson, T.E., Granados-Riveron, J., Udosen, I., Morris, G.E., Holt, I., Furling, D., et al. (2014). High-content screening identifies small molecules that remove nuclear foci, affect MBNL distribution and CELF1 protein levels via a PKC-independent pathway in myotonic dystrophy cell lines. Hum. Mol. Genet. *23*, 1551–1562. https://doi.org/10.1093/HMG/DDT542.

42. Bjørkøy, G., Lamark, T., Pankiv, S., Øvervatn, A., Brech, A., and Johansen, T. (2009). Monitoring autophagic degradation of p62/SQSTM1. Methods Enzymol. *452*, 181–197. https://doi.org/10.1016/S0076-6879(08)03612-4.

43. Raben, N., Shea, L., Hill, V., and Plotz, P. (2009). Monitoring Autophagy in Lysosomal Storage Disorders. Methods Enzymol. *453*, 417–449. https://doi.org/10.1016/S0076-6879(08)04021-4.

44. Yablonka-Reuveni, Z., and Nameroff, M. (1990). Temporal differences in desmin expression between myoblasts from embryonic and adult chicken skeletal muscle. Differentiation. *45*, 21–28. https://doi.org/10.1111/J.1432-0436.1990.TB00452.X.

45. Peng, X., Shen, X., Chen, X., Liang, R., Azares, A.R., and Liu, Y. (2015). Celf1 regulates cell cycle and is partially responsible for defective myoblast differentiation in myotonic dystrophy RNA toxicity. Biochim. Biophys. Acta *1852*, 1490–1497. https://doi.org/10.1016/J.BBADIS.2015.04.010.

46. Gambardella, S., Rinaldi, F., Lepore, S.M., Viola, A., Loro, E., Angelini, C., Vergani, L., Novelli, G., and Botta, A. (2010). Overexpression of microRNA-206 in the skeletal muscle from myotonic dystrophy type 1 patients. J. Transl. Med. *8*, 48. https://doi.org/10.1186/1479-5876-8-48.

47. Hon, L.S., and Zhang, Z. (2007). The roles of binding site arrangement and combinatorial targeting in microRNA repression of gene expression. Genome Biol. *8*, R166. https://doi.org/10.1186/GB-2007-8-8-R166.

48. Fardaei, M., Larkin, K., Brook, J.D., and Hamshere, M.G. (2001). In vivo co-localisation of MBNL protein with DMPK expanded-repeat transcripts. Nucleic Acids Res. *29*, 2766–2771.

49. Pettersson, O.J., Aagaard, L., Jensen, T.G., and Damgaard, C.K. (2015). Molecular mechanisms in DM1 - a focus on foci. Nucleic Acids Res. *43*, 2433–2441. https://doi.org/10.1093/nar/gkv029.

50. Michlewski, G., and Cáceres, J.F. (2019). Post-transcriptional control of miRNA biogenesis. RNA *25*, 1–16. https://doi.org/10.1261/rna.068692.118.

51. Zhang, S., and Chen, N. (2018). Regulatory Role of MicroRNAs in Muscle Atrophy during Exercise Intervention. Int. J. Mol. Sci. *19*, 405. https://doi.org/10.3390/IJMS19020405.

52. Safdar, A., Abadi, A., Akhtar, M., Hettinga, B.P., and Tarnopolsky, M.A. (2009). miRNA in the Regulation of Skeletal Muscle Adaptation to Acute Endurance Exercise in C57Bl/6J Male Mice. PLoS One *4*, e5610. https://doi.org/10.1371/journal.pone.0005610.

53. Song, K.-Y., Guo, X.-M., Wang, H.-Q., Zhang, L., Huang, S.-Y., Huo, Y.-C., Zhang, G., Feng, J.-Z., Zhang, R.-R., Ma, Y., et al. (2020). MBNL1 reverses the proliferation defect of skeletal muscle satellite cells in myotonic dystrophy type 1 by inhibiting autophagy via the mTOR pathway. Cell Death Dis. *11*, 545. https://doi.org/10.1038/s41419-020-02756-8.

54. Roussel, M.-P., Ravel-Chapuis, A., Gobin, J., Jasmin, B.J., Leduc-Gaudet, J.-P., Gagnon, C., and Duchesne, E. (2024). Changes in Physiopathological Markers in Myotonic Dystrophy Type 1 Skeletal Muscle: A 3-Year Follow-up Study. J. Neuromuscul. Dis. *11*, 981–995. https://doi.org/10.3233/JND-230139.

55. Hu, M., Ge, M.-R., Li, H.-X., Zhang, B., and Li, G. (2022). Identification of DAPK1 as an autophagy-related biomarker for myotonic dystrophy type 1. Front. Genet. *13*, 1022640. https://doi.org/10.3389/fgene.2022.1022640.

56. Leduc-Gaudet, J.-P., Franco-Romero, A., Cefis, M., Moamer, A., Broering, F.E., Milan, G., Sartori, R., Chaffer, T.J., Dulac, M., Marcangeli, V., et al. (2023). MYTHO is a novel regulator of skeletal muscle autophagy and integrity. Nat. Commun. *14*, 1199. https://doi.org/10.1038/s41467-023-36817-1.

57. Loro, E., Rinaldi, F., Malena, A., Masiero, E., Novelli, G., Angelini, C., Romeo, V., Sandri, M., Botta, A., and Vergani, L. (2010). Normal myogenesis and increased apoptosis in myotonic dystrophy type-1 muscle cells. Cell Death Differ. *17*, 1315–1324. https://doi.org/10.1038/CDD.2010.33.

58. Morriss, G.R., Rajapakshe, K., Huang, S., Coarfa, C., and Cooper, T.A. (2018). Mechanisms of skeletal muscle wasting in a mouse model for myotonic dystrophy type 1. Hum. Mol. Genet. *27*, 2789–2804. https://doi.org/10.1093/HMG/DDY192.

59. Krol, J., Loedige, I., and Filipowicz, W. (2010). The widespread regulation of microRNA biogenesis, function and decay. Nat. Rev. Genet. *11*, 597–610. https://doi.org/10.1038/nrg2843.

60. Lee, K.-H., Lotterman, C., Karikari, C., Omura, N., Feldmann, G., Habbe, N., Goggins, M.G., Mendell, J.T., and Maitra, A. (2009). Epigenetic Silencing of MicroRNA miR-107 Regulates Cyclin-Dependent Kinase 6 Expression in Pancreatic Cancer. Pancreatology *9*, 293–301. https://doi.org/10.1159/000186051.

61. Overby, S.J., Cerro-Herreros, E., Espinosa-Espinosa, J., González-Martínez, I., Moreno, N., Fernández-Costa, J.M., Balaguer-Trias, J., Ramón-Azcón, J., Pérez-Alonso, M., Møller, T., et al. (2023). BlockmiR AONs as Site-Specific Therapeutic MBNL Modulation in Myotonic Dystrophy 2D and 3D Muscle Cells and HSALR Mice. Pharmaceutics *15*, 1118. https://doi.org/10.3390/PHARMACEUTICS15041118.

62. Bolger, A.M., Lohse, M., and Usadel, B. (2014). Trimmomatic: a flexible trimmer for Illumina sequence data. Bioinformatics *30*, 2114–2120. https://doi.org/10.1093/BIOINFORMATICS/BTU170.

63. Wu, T., Hornsby, M., Zhu, L., Yu, J.C., Shokat, K.M., and Gestwicki, J.E. (2023). Protocol for performing and optimizing differential scanning fluorimetry experiments. STAR Protoc. *4*, 102688. https://doi.org/10.1016/J.XPRO.2023.102688.

64. Schindelin, J., Arganda-Carreras, I., Frise, E., Kaynig, V., Longair, M., Pietzsch, T., Preibisch, S., Rueden, C., Saalfeld, S., Schmid, B., et al. (2012). Fiji: an open-source platform for biological-image analysis. Nat. Methods *9*, 676–682. https://doi.org/10.1038/nmeth.2019.